Master's thesis

NTNU
Norwegian University of Science and Technology
Faculty of Engineering
Department of Mechanical and Industrial Engineering

Peder August Håøya

Post-tension as a mechanical solution to improve FFF Z-strength: A quantitative research on how post-tension affects static strength and fatigue life for PETG specimens in three-point bending tests

Master's thesis in Produktutvikling og Produksjon
Supervisor: Christer Westum Elverum
Co-supervisor: Seyed Mohammad Javad Razavi
May 2022

NTNU
Norwegian University of
Science and Technology

Peder August Håøya

Post-tension as a mechanical solution to improve FFF Z-strength: A quantitative research on how post-tension affects static strength and fatigue life for PETG specimens in three-point bending tests

Master's thesis in Produktutvikling og Produksjon
Supervisor: Christer Westum Elverum
Co-supervisor: Seyed Mohammad Javad Razavi
May 2022

Norwegian University of Science and Technology
Faculty of Engineering
Department of Mechanical and Industrial Engineering

NTNU
Norwegian University of
Science and Technology

Post tension as a mechanical solution to improve FFF Z-strength: A quantitative research on how post-tension affects static strength and fatigue life for PETG specimens in three-point bending tests

Peder August Håøya

May 2022

Master Thesis

Department of Mechanical and Industrial Engineering

Norwegian University of Science and Technology

Supervisor 1: Christer Westum Elverum

Supervisor 2: Seyed Mohammad Javad Razavi

Abstract

Parts made by fused filament fabrication (FFF) are weaker in the build direction, referred to as Z-strength. This is mainly due to the weaker fusion zones between printed layers. To reduce this problem has extensive research been done by optimizing printing parameters. Little research has been done on improving Z-strength by introducing mechanical solutions such as post-tension. This research aims to investigate and document the effect post-tension has on improving Z-strength in specimen made by FFF.

Static and fatigue three-point bending tests were performed on specimens, printed with PETG in the upright direction, tested with and without post-tension. Tests were performed with post-tension placed in the neutral axis (center) and in the bottom of the specimens. Fatigue tests were performed at normalized loads based on experimental results from static tests.

Static test results shows increased maximum load of 5.6% for center post-tension and 34.8% for bottom post-tension specimen. Fatigue tests results shows an average increase in fatigue life for center post-tension by a factor of 5.8 to 14.4. Bottom post-tension specimen loaded at the highest normalized load (76.3%) were further increased by a factor of 2.5 compared with center post-tension specimen. At loads below 66.8% of maximum static load did bottom post-tension specimen achieve runout results and were stopped after 1 million cycles.

The results from this research documents that post-tension can be used as a mechanical solution to improve the Z-strength in parts made by FFF.

Contents

Chapter 1

Introduction

Fused filament fabrication (FFF) is an additive manufacturing (AM) process where the printed parts are created by building one layer at a time. It was developed in the 1980s and used for nonfunctional prototypes in product development. With research and technological development of machines and materials has the usability of parts made by FFF increased. Prototyping is one of the main areas for FFF, due to the benefits the method provides within design freedom, automation, lead time and low production cost of small batches, compared to traditional manufacturing methods. One of the main drawbacks with FFF is the anisotropic mechanical properties. This is a result of parts being made layer by layer and that the bonding zone between each layer are weaker than the material itself, making parts made by FFF prone to failure due to tensile stresses in the build direction, often referred to as Z-strength. In attempts to reduce this weakness has extensive research been done related to optimizing printing parameters. Little research has been done investigating mechanical solutions such as post-tension. To the best of our knowledge is there currently no widely available papers on the use of post-tension in small to medium size AM components. Post-tension has been used in joining of big area additive manufactured (BAAM) components and in multiple applications of 3D concrete printing (3DCP). This research will investigate the possible benefits post-tension has on Z-strength in parts made by FFF.

1.1 Research aim and objectives

The effect of using post-tension to improve strength in FDM components is poorly studied with little research available.

The aim of this thesis is to investigate and document the effect of using post-tension to improve Z-strength in FDM specimens.

The research aim is documented according to objectives 1-8 below. The objectives are executed sequential in three phases shown as A-C below and further evaluation and discussion in phase D.

Phase A - Design and work-plan objectives:

1. Design specimen with simple internal geometry and approximate 2.5h print time. This is to enable production of a statistical relevant number of test specimens, within available time.

2. Develop a reliable post-tension system that enables predictable tension in all specimens. This is to ensure comparability between test specimens.

Phase B - Theoretical calculations and numerical modeling objectives:

3. Perform theoretical calculations to estimate strength of the specimen without post tension. Results are compared with experimental and simulated values.

4. Establish applied compression force on test specimen by performing theoretical calculations on post-tension system. Results are used in point 5.

5. Create a numerical model to establish theoretical strength of the specimen with post tension values from theoretical calculations (point 4).

Phase C - Experimental test objectives:

6. Document static bending strength for the different scenarios by conducting three-point bending tests.

7. Document fatigue life of the different scenarios by conduction fatigue three-point bending tests at normalized loads based on static performance.

8. Document simple fractography to investigate post tension effect on fracture surface.

   Phase D - Evaluate and discuss results documented in phase A-C.

Chapter 2

Theoretical background

2.1 Fused filament fabrication

Fused filament fabrication (FFF, Figure 2.1) is an AM process in which a filament is heated and extruded onto a build plate while moving in the XY-plane, after the pre programmed 2D geometry is made the nozzle moves up in the Z-direction and a new layer is deposited. Several 2D geometries stacked on top of each other forms the desired 3D shape. The most common materials are thermoplastics which usually are stored as rolls of filament. As the filament is pushed through the nozzle it is heated close to its melting temperature were it turns into a rubbery state, making it ductile and able to attach to the build plate or fuse to the previous layer. This causes a fusion zone between each layer, were mechanical properties are weaker. This makes components made with FFF anisotropic.

2.1.1 Copolymer - PETG

Polyethylene Terephthalate (PET) is a widely used polymer used for packaging (e.g. plastic bottles) and textiles, then referred to as polyester. Chemical modification (co-polymerization) of the PET polymer result in PETG (polyethylene terephthalate glycol-modified). This amorphous thermoplastic is a commonly used in FFF 3D-printing.

The chemical difference between PET and PETG's is that cyclohexane-dimethanol (CHDM)

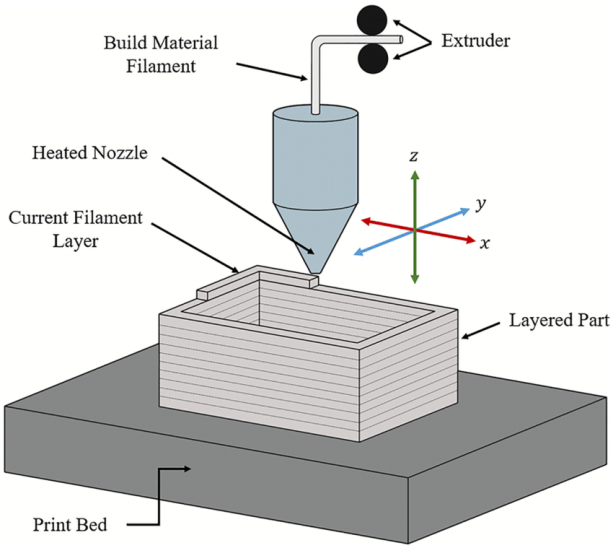

Figure 2.1: A schematic illustration of the fused filament fabrication process (J. Shah & Hosseini (2019)).

replace ethylene glycol in PET. Since CHDM is a much larger building block than ethylene glycol it does not fit in with the neighboring chains the same way as in PET (Matmatch (2020)). The larger building block reduces melting temperature of PET and interferes with crystallization, making PETG amorphous were PET is semi-crystalline.

3D-printer manufacturer Prusa Research (2021) state that if strength and toughness is most important it is recommended to turn off the printing fan and increasing nozzle temperature to improve the fusion between layers. As most 3D-printing filaments do PETG absorb moisture from the environment. When the absorbed moisture in the filament is heated in the nozzle it turns into gas and expands, causing inconsistent extrusion, bobbles, bad surface finish and weaker layer adhesion. These negative effects can be reduced by drying the filament before use. PETG's glass transition temperature is around 80°C to 85°C. PETG's do not have a distinct melting temperature due to its amorphous structure. Transition into a more liquid state starts around 230°C, melting point is often refereed to be approximate 250C.

2.1.2 Layer and inter-layer bonding

The strength and degree of anisotropy of FFF components are dependent on the bonding between each layer. This is especially true for Z-strength, as the whole cross section normal to the Z-direction is a fusion zone. The bonding process in FFF may, as shown in Figure 2.2 be divided into three steps:

1. Surface contact between the previous and new layer.
2. Neck growth where the two layers fuse into each other.
3. Molecular diffusion of polymer chains across the neck.

According to Yin et al. (2018) is the bonding strength dependent on two factors. Neck growth and degree of molecular diffusion between two layers. Better neck growth causes larger fused cross section area. The degree of molecular diffusion increases the mechanical strength of the bond. The diffusion takes place as long as the temperature stays above the glass transition temperature, and according to Xunfei Zhou (2017) the longer temperature stay above glass transition temperature stronger the bonds become.

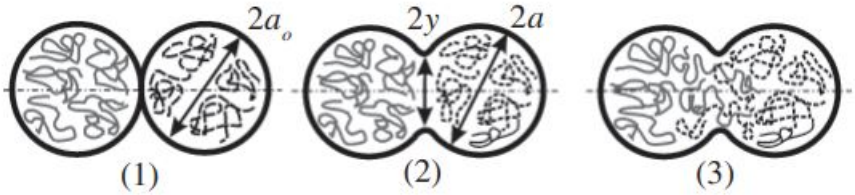

Figure 2.2: The cross-sections of filaments are idealized as circles, (1) surface contact, (2) neck growth, (3) molecular diffusion (Céline Bellehumeur (2004)).

2.1.3 Internal defects

The presence of internal defects is an important factor that affect the strength of FFF printed components. The FFF process leads to higher concentrations of defects in the section between layers in the part. These sections are weaker as they are fusion zones with worse mechanical

properties than the base material. Crack initiation can therefor often be traced back to internal defects between layers. Defects in FFF prints can roughly be divided in to two categories, systematic defects and random defects.

Systematic defects are defects that are results of programmed nozzle-path and printing parameters. These defects would appear similarly in the same spots if components are printed multiple times with the same printing parameters. These are defects such as voids, seams and different gaps. The majority of systematic voids in FFF prints are formed due to the elliptic cross section of the deposited filament, as seen in Figure 2.3. Seams appears in sections where the material extrusion starts and stops in the building process, creating a seam with a fusion zone where material properties are weaker. Gaps are sections in the plane where the deposited filament is not in contact with the surrounding filament, causing an internal gap. This can appear in several forms and is often a result of under extrusion.

Defects appears randomly in the print. Nozzle build-up that deposited between layers is one type of random defect that can cause a significant weakness in the print. Another cause of internal defects can be inconsistent extrusion of filament, this can be a due of several reasons. It can be due to low-quality filament with variable thickness, change in temperature of the deposited filament or filament with absorbed moisture causing gas bobbles. In addition to causing inconsistent extrusion is gas bobbles in the filament and between layers another type of random defect.

Optimizing printing parameters have shown to reduce size and number of defects Ferretti et al. (2021), which result in improved strength.

2.1.4 The effect of printer parameters and part orientation

Printer parameters affects the strength of the fusion zone between layers, and part orientation affects to what degree the tensile strength is affected by the layer strength.

Printer parameters that has the largest impact on strength are infill, nozzle temperature, print bed temperature, extrusion rate, layer thickness, printing speed and fan speed.

Infill can be set from 0%, which will result in a shell component, to 100% infill which will

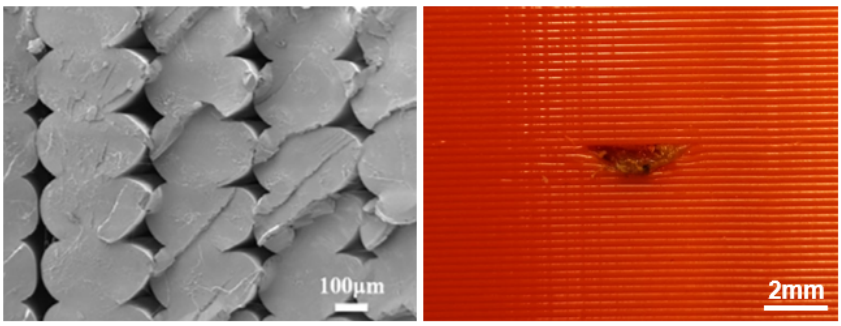

Figure 2.3: Left image shows systematic defect in the form of continuous voids (Mehdikhani et al. (2019)). Right image shows random defect due to nozzle buildup.

result in a solid component. Between those values a partly hollow structure will be created. Different patterns can be assigned for this structure with different benefits related to strength and print time. More infill leads to higher strengths, due to a larger cross sectional area. Higher nozzle temperature leads to stronger bonding between layers, due to higher degree of inter-layer diffusion as stated in 2.1.2. Precision is reduced at higher temperature. For Prusament PETG the recommend temperature is 250°C ± 10°C, where the lower range should be used if details are most important, higher range for strength and middle range for balance between the two. Having a heated print bed decreases cooling which increases interlayer bonding. The print bed temperature should be at, or just below, the glass transition temperature. This is to keep the part solid at the same time as heat gradient is as low as possible which improves/increases interlayer bonding. Extrusion rate is the volumetric flow rate of the filament. Increasing it leads to more material being deposited. This results in larger bonding area and smaller voids leading to higher strength. This comes at the cost of worse accuracy and surface finish. Larger layer thickness has shown to reduce strength and Young's modulus as the results from Zhao et al. (2019) shows, which also can be seen as seen in Figure 2.5. The printing speed together with layer area determines the time between each layer is deposited. Less cooling of the previous layer increases bonding strength, as was documented by Vladimir E. Kuznetsov (2019). For this reason will increased fan speed reduce strength as it cools down the previous layer. Figure 2.4 shows some of the main findings from Vladimir E. Kuznetsov (2019). The research state that two of the main parameters that effect mechanical strength of FFF components is extrusion efficiency E_E and

sub layer temperature t_{sub}. Extrusion efficiency is the ratio between actual extruded material and estimated amount calculated by the slicer software. Sub layer temperature is the temperature of previous laid layer in the FFF process. Both leads to an increase in strength given as ultimate failure stress (UFS) in the graph. Which of the investigated printer parameters that had a positive or negative effect on E_E and t_{sub} can be seen in the flow chart to the left in the figure.

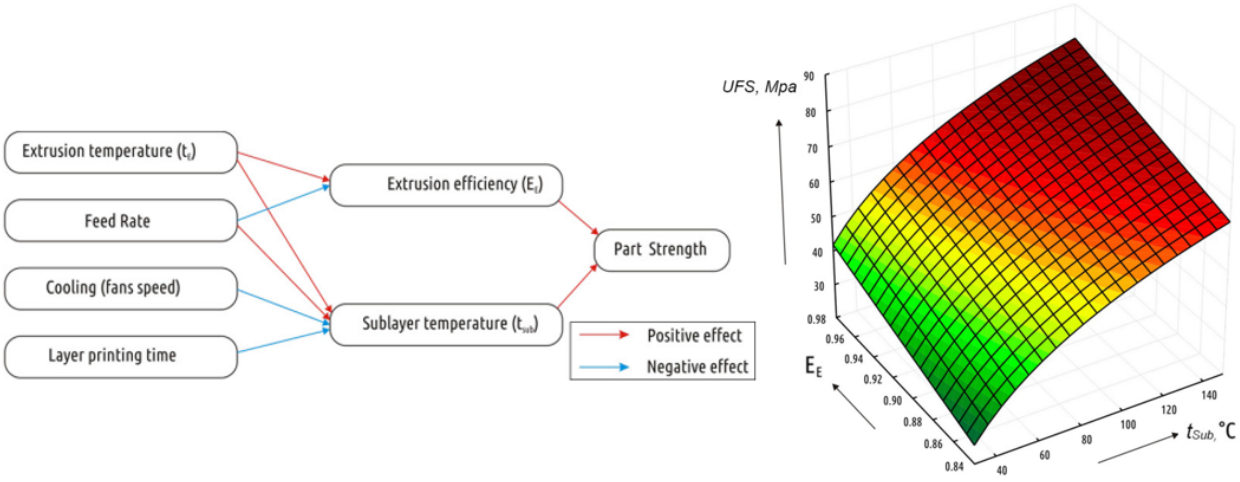

Figure 2.4: Flow chart of printing parameters effect on part strength, and surface showing effects of parameter extrusion efficiency and sublayer temperature on ultimate failure stress (Vladimir E. Kuznetsov (2019)).

Research on the effect of printing angle and layer thickness on strength and Young's modulus of PLA FFF material were conducted by Zhao et al. (2019). It shows that specimens get a decrease in Youngs modulus and becomes weaker with increased layer thickness and lower printing angles. With a layer thickness of 0.3mm is the tensile strength of the 0°(upright direction) material only 43% of the 90°(horizontal) material. At 0°has specimens with layer thickness of 0.3mm 18% lower tensile strength than 0.1mm and 10% lower than 0.2mm. Young's modulus for 0.3mm specimens are 25% less than 0.1mm and 13% less that 0.2mm.

2.2 Bending and tensile strength

Materials that are weaker in tension than in compression fail due to tension stresses in both a bending test and a tensile test. However, due to the stress state and the critical volume, will

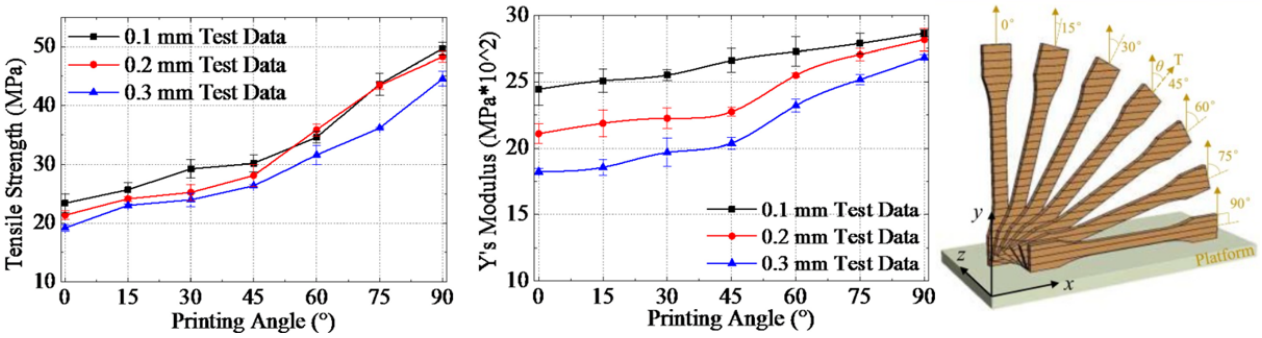

Figure 2.5: Tensile strength and Young's modulus related to printing angle and layer thickness (Zhao et al. (2019)).

the values of maximum tensile stresses be different in the two tests. Materials can take larger stresses in three-point bending due to the smaller critical volume. In a three-point bending test is the critical volume of the highest tensile stresses, conversely concentrated in a small region at the opposite side of where the load from the loading pin is being applied to the specimen. In a tensile test is the stresses distributed relatively uniformly over the entire gauge width and length. For this reason is the critical volume much larger, given that the specimen in bending and tensile tests are approximately the same size. Because of the larger critical volume is the probability of a critical defect therefor larger in tensile test. As a result is it expected that ultimate tensile stress obtained from 3-point bending is higher than the ultimate tensile stress obtained from tensile test, even if the materials have equal strength. The same results were found by Chacón et al. (2017) when testing FFF PLA specimen in weak axis. The samples printed in the upright direction with a layer thickness of 0.24mm and printing speed of 80mm/s failed on average at 28.4 MPa in tensile test and 39.5 MPa in bending test. This being a 28% reduction in obtained ultimate tensile stress from specimen tested in tensile test.

2.3 Fractography

Fractography is the study of the micro structure in the fracture surfaces, it can be used to determine the root of the fracture and failure mechanism. Relevant for this study is the characteristics of rib-marks. These curved crack front markings appear due to sudden changes in crack veloc-

ity of the crack tip. Rib-marks has some of the same characteristics as fatigue striations, but are usually larger and are not result of cyclic loading. For both fatigue striations and rib-marks the fraction origin is on the concave side of the markings. An example of rib-marks from a point load failure in HDPE pipe can be seen in Figure 2.6.

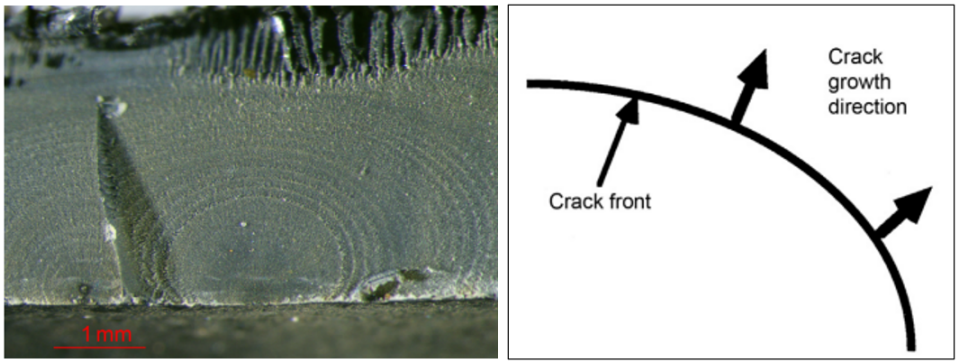

Figure 2.6: Point load failure in HDPE pipe showing rib markings curving inward toward inner surface and schematic illustration of rib markings showing crack growth direction (Hayes et al. (2015)).

2.4 Post-tension

Theory and information used in this section is from "Post-Tensioning Tendon Installation and Grouting Manual" by the U.S. Department of Transportation (John Corven, P.E. and Alan Moreton, P.E (2013)).

The use of post-tension was one of the major advancements in bridge construction in the second half of the twentieth century. When using post-tension is the reinforcement added to open channels after the structure has hardened unlike reinforcement by pre-tension or rebars. Concrete gain large benefits from post-tension due to its tensile strength being only 10% of its compressive strength. By inducing large compressive stresses with post tension to the structure before loads are applied one can reduce or eliminate tensile stresses in the concrete as illustrated by superposition principle in Figure 2.7. The total strength is not necessarily increased compared to using rebars. However, it reduces the amount of cracks and micro cracks resulting

in a more durable design. Another important benefit with post-tension in bridge construction is control of deflection. The position of the post-tension steel-wires in cross section effect specimen bending and to what degree the load is held by the wires, in a three-point bending case. Having the post-tension wire along the neutral axis of a beam it will stay straight. In the case of bending due to an external load will the length of the neutral axis stay constant, and post-tension force will stay the same as long as the integrity of the material stays the same. Placing post-tension in the lower section of a beam will result in bending upwards before external load is applied. Ideally does the bending from post-tension and from the external force balance each other out resulting in a straight beam with reduced tensile stresses. If the external load is further increased in the beam with post tension off-center will the stress in the post tension wires further increase.

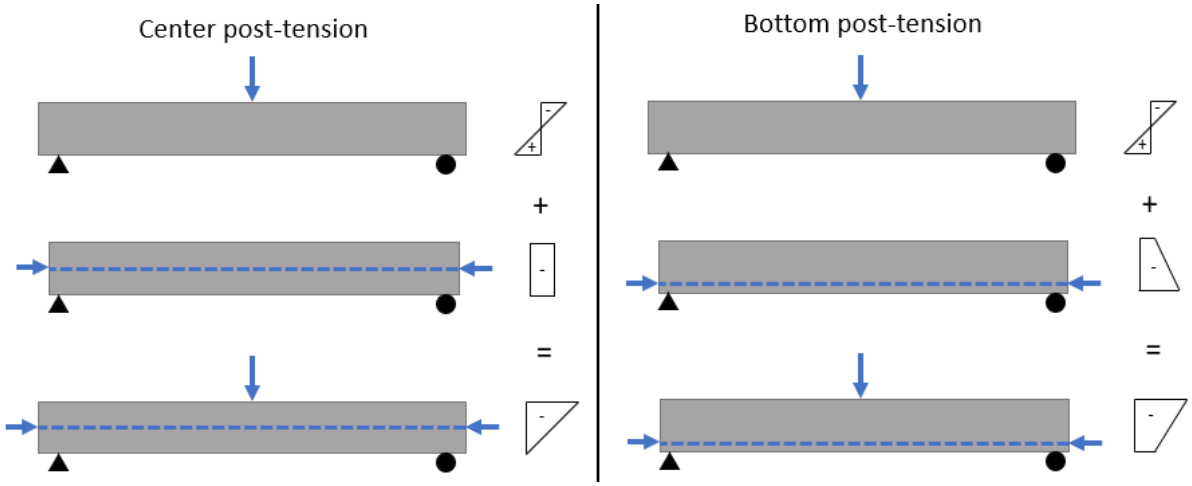

Figure 2.7: Superposition principle of center and bottom post tensioned beam in three-point bending.

2.4.1 Post-tension in AM

There is no widely available research on post tension used in small to medium scale AM components to the best of our knowledge. However, there have been some research on larger structures made with 3D concrete printing (3DCP) and big area additive manufacturing (BAAM) using polymers. In these cases it have been used to enhance z-strength and to strengthen the

joining mechanism in the assembly of smaller components.

Concrete bridge

In one proof-of-concept study performed at Department of Structural Engineering at Ghent University a 3DCP bridge were created using topology optimization and post-tension wires Vantyghem et al. (2020). Their findings showed an approximately 20% material savings compered to a T-section girder with the same strength. The result can be seen in figure 2.8.

Hyperion Robotics is a company in Helsinki who also have used 3DCP and post tension. They claim that "By placing material where it is most needed, and creating catenary shaped conduits for the post-tensioning rods, we have been able to save 50% of material compared to a traditional RC beam of similar bending strength"(Hyperion-Robotics (2021)). Indicating large material savings by utilizing 3DCP and post tension.

Figure 2.8: AM post-tensioned bridge from Ghent University (Vantyghem et al. (2020)).

Boat Mold

Post et al. (2018) studied the use of post-tension in BAAM, this was done as a collaboration between Oak Ridge National Laboratory and Alliance MG. They explored the feasibility of using parts created with BAAM to manufacture a 11-meter boat mold with minimal post processing. The mold consisted of 12 parts that were glued with epoxy and clamped together using 10 steel rods. The tension was applied using nuts and washers. The load was distributed to the polymer mold through springs and aluminum bulkheads on each side to reduce stress concentrations at

the connection point between rod and mold. Their result showed that it was possible to print a self-supporting large-scale mold with the use of several smaller printed parts and post-tension.

Figure 2.9: A 11-meter long post-tensioned boat mold consisting of 12 parts made by BAAM(Post et al. (2018)).

Chapter 3

Methods

3.1 Phase A - Design of specimen and post-tension system

3.1.1 Specimen design and preparation

The requirement of the specimen was to have channels for the post-tension wires and space for different placements of these along the vertical axis. To be able to produce sufficient sample size it was required that printing time were not to long. Specimen needed to withstand stresses from loading-pin without failure occurring at contact point. For these reasons standard specimen for three-point bending was not used. The specimen were designed to be partly hollow with support in the vertical direction with wire channels on the side of these supports. The length of the specimen were set to 120mm to fit the 100mm support span, cross-sectional geometry and dimensions were as in Figure 3.1. The reason for not printing a solid rectangular with channels is that it would require significantly longer print time. FFF components often do not use solid internal geometry. Partly hollow geometry would likely highlight the benefits with post tension as steel wire becomes a larger part of the cross section. Several wall thicknesses and internal geometry designs were tested in the pursuit to find a design that would take the load in three-point bending without large deformations at the contact point between specimen and loading pin. Testing proved that with a thickness of 1.2mm resulting in three lines of 0.4mm filament the post tension specimen was strong enough so that the loading-pin would not penetrate the

top surface during testing, which was the case for the specimen with thinner wall thickness. To get a sufficiently low printing time were the layer height increased from 0.2mm to 0.3mm.

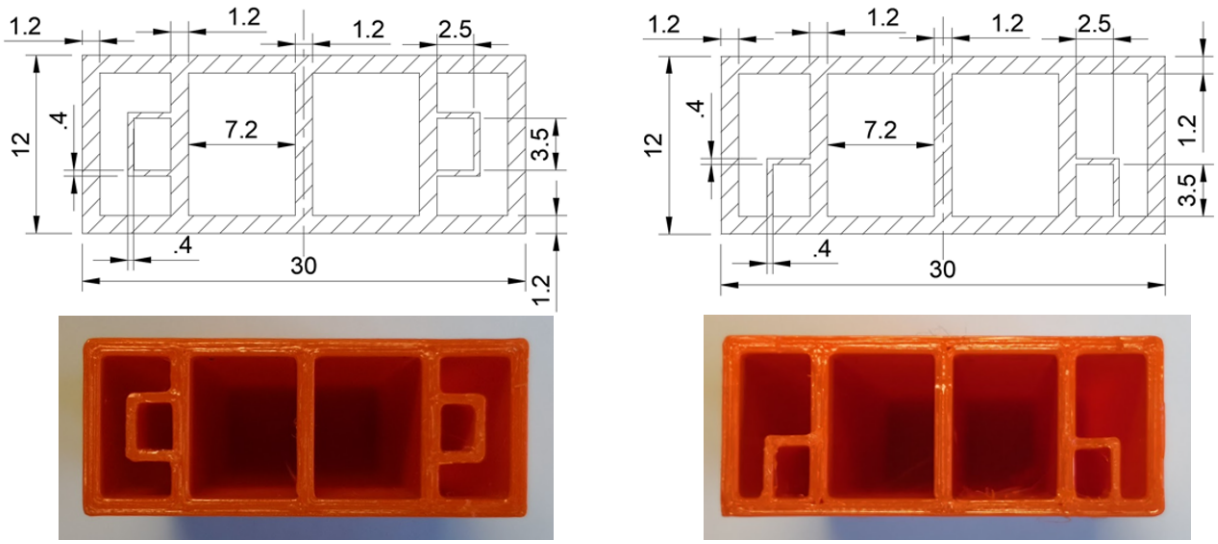

Figure 3.1: Technical drawing and images of specimens cross sections. Specimens are closed at each end and has a length of 120mm.

3.1.2 Printer, settings and material

All specimen were produced using an Original Prusa i3 MK3S+ with a 0.4 nozzle. This printer has a heated bed and prints were performed in room temperature at 20±2 °C. Specimens were printed one at a time to ensure equal time between each layer deposition for each specimen. The geometries were designed in Autodesk Fusion 360 before it were converted in to a STL-files. These files were then imported to PrusaSlicer. In PrusaSlicer the specimen were placed to be printed upright with printer settings set to "0.2mm QUALITY", layer height was increased to 0.3mm to reduce print time. Main printing parameters can be seen in Table 3.1.

The filament used was PETG Prusa orange. The rolls of filament was stored in room temperature and were not dried before use. Mechanical properties from Prusa are listed in Table 3.2.

Table 3.1: Main printer parameters used in production of specimen for this experiment, and printer parameters used in Prusas experiment to conduct material properties for PETG technical data sheet listed in Table 3.2 (Prusa Polymers).

	This experiment	Prusa experiment	Unit
Layer hight	0.3	0.2	mm
Nozzle temperature	240	260	°C
Bed temperature	90	90	°C
Infill	100	100	%
Extrusion multiplier	1.00	1.07	
Infill print speed	80	100	mm/s

Table 3.2: Mechanical properties of PETG filament printed in different orientations.(Prusa Polymers).

Material	Horizontal (MPa)	Vertical X, Y-Axis (MPa)	Vertical Z-axis (MPa)	Method
PETG	47±2	50±1	30±5	ISO 527-1

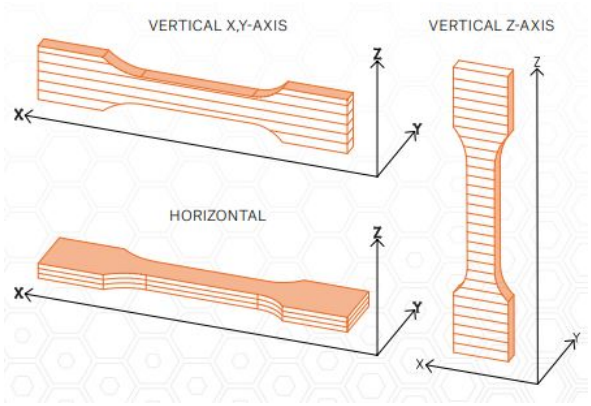

Figure 3.2: Illustration of Prusa dog bone specimen with print direction (Prusa Polymers).

3.1.3 Post-tension system

The post-tension system has three main functions:

1. PT-system must be adjustable to same tension each time it is mounted
2. Tension forces that distributes during the testing must be comparable
3. Mounting must be predictable, quick mounted and relative compact

In an attempt to solve these requirements a post tension system with wire clamps and hollow bolts were made. Aluminium plates with holes were cut and used with bolts to create wire clamps. The hollow bolts were made out of M10 bolts as it was the smallest bolt which it was feasible to drill a hole with the available lathe and drill-head in the workshop. The first wire clamps were made with M3 bolts and nuts, these were later changed to M5 as the M3 bolts would fail while tightening after a few tests. The M5 bolts held up well. The tension is applied by inserting wire in both channels in the specimen, then having a bracket on each side of the specimen fitting the wire clamps and bolts. The hollow bolts with nuts are placed on one side and then both ends of the wire is clamped with the aluminium plates. Tension can then be applied by rotating the bolt while holding the nut. The tension can be controlled by first tightening the nuts with the fingers to get a snug fit, then using a wrench a given number of rotations. For the center post specimens the bolt was given 1.5 rotation for the bottom post specimen the bolt was given 1.25 rotation. One rotation of the M10 bolt equals its pitch of 1.5mm in linear movement. The reason for the difference in rotations is that first experiments were conducted on center specimens with 1.5 rotations, applying the same amount to bottom channeled specimen led to large deflections. To reduce the risk of failure in the top section during fatigue testing, the wire tension was slightly reduced. The wires used for post tension were made of stainless steel and had a diameter of 1.2mm.

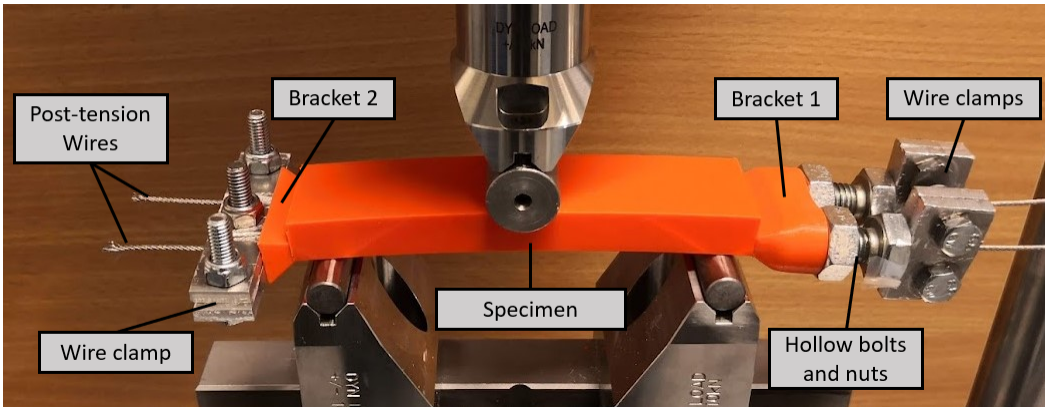

Figure 3.3: Post-tension setup of specimen in three-point bending.

3.2 Phase B - Calculations and modeling

3.2.1 Stress analysis of control specimen

Theoretical calculations were performed to compare the theoretical strength to the experimental results and the results from the numerical model. It is assumed failure due to maximum principal stress, given by equation 3.1. The stresses in the cross section of a specimen in three point bending is in the form of normal stresses and shear stresses. Normal stresses increase linearly with distance from neutral axis, shear stress has maximum value in the neutral axis and most of the shear stresses is in the vertical section of a partly hollow rectangular as seen in Figure 3.4. In three point bending were h/L=<0.10 (h=height, L=length) can it be assumed that failure is due to maximum normal stresses, and that shear stresses can be neglected. In this experiment of partly hollow specimen with a h/L ratio of 0.12 is shear stresses still neglected and failure assumed to be due to normal stresses. The assumption were controlled in the numerical model. Failure is assumed to be due to tension, stress calculations is therefor performed on the bottom section of the specimen. A total of three different cross section are used in this thesis, without wire channels as in Figure 3.4) and with wire channels in the center and at the bottom as in Figure 3.1. The theoretical maximum load in three-point bending can be calculated from beam theory and the given ultimate tensile stress (UTS). By using equations for maximum principal stress Equation 3.1, second moment of area by Steiner's theorem Equation 3.2, maximum moment Equation 3.3 and formula for maximum bending stress Equation 3.4. This gives the Equation 3.5 for theoretical maximum three-point bending loads.

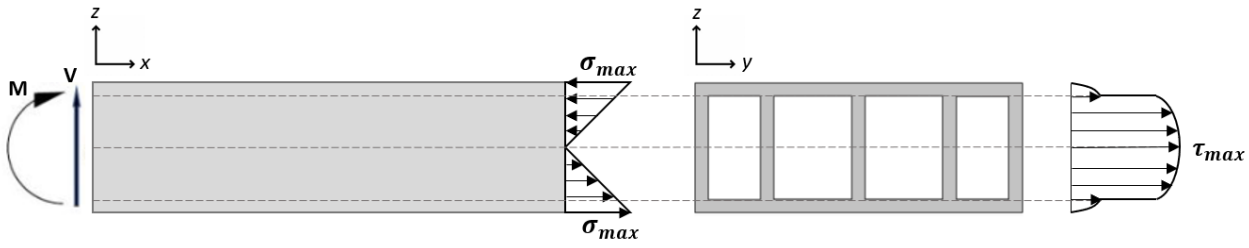

Figure 3.4: Schematic illustration of bending and shear stress in specimen without wire channels. σ=normal stress in X-direction, τ=share stress in YZ-plane, M=moment and V=share stress.

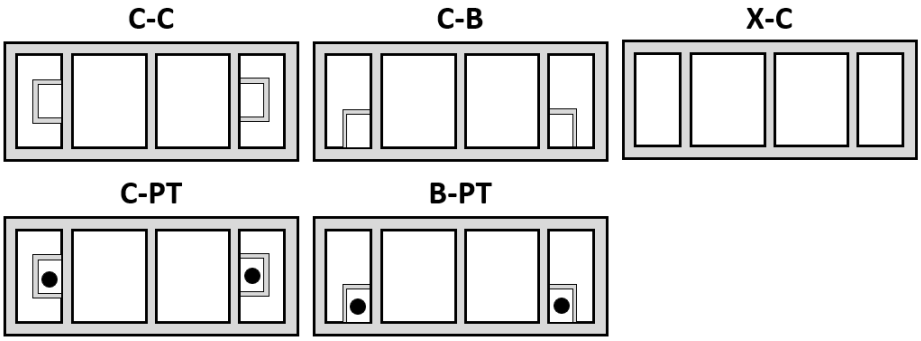

Figure 3.5: Naming of the different cross sections used in calculations and experiments. Post-tension wires are marked as black circles. Relative dimensions are not presented accurate.

$$\sigma_{1,2} = \frac{\sigma_x + \sigma_y}{2} \pm \sqrt{\frac{\sigma_x^2 - \sigma_y^2}{2} + \tau_{xy}^2} \tag{3.1}$$

$$I_y = \sum I_{yi} + z_i^2 \cdot A_i \tag{3.2}$$

$$M_{max} = \frac{F \cdot L}{4} \tag{3.3}$$

$$\sigma_{max} = \frac{M_{max}}{I_y} \cdot z \tag{3.4}$$

$$\Rightarrow$$

$$F_{max} = \frac{4 \cdot I_y \cdot \sigma_{max}}{L \cdot z} \tag{3.5}$$

3.2.2 Compression force from post tension

The theoretical magnitude of the compression force from the post tension system can be calculated using spring theory. All components in the system are seen as a series of springs with equal forces acting between them. The system consist of two 1.2mm steel wires, two hollow M10 bolts with nuts, wire clamps, bracket for the bolts and bracket for clamps. When calculating the

theoretical force from post tension it is assumed that:

- Bolts and nuts are perfectly rigid
- Constant cross section of the brackets equal average cross section based on total volume and height from CAD model
- Constant cross section of specimen equal average cross section of center and bottom channeled specimen
- No deflection in specimen
- FFF PETG is a linear isotropic Hookean material
- Finger pre-tightening of nuts leads to neutral stress state in the wires (before wrench is used)

The force is then calculated by using Hooke's law Equation 3.6, stiffness formula Equation 3.7, formula of linear bolt motion based on rotations Equation 3.8 and Newtons third law Equation 3.9. Total elongation and compression of the components in the post tension system must be equal to the linear motion of the bolt due to the rotations of the nuts. The force is equal between every component in the system. Hence can the force be given by Equation 3.10.

$$F = k \cdot \Delta l \tag{3.6}$$

$$k = \frac{A \cdot E}{l} \tag{3.7}$$

$$\sum \Delta l = n_{nut-rotations} \cdot l_{bolt-pitch} \tag{3.8}$$

$$F_{AB} = -F_{BA} \tag{3.9}$$

$$\Rightarrow$$

$$\Delta l_{tot} = \frac{F_i}{k_i} = F \cdot \sum \frac{1}{k_i}$$

$$F = \Delta l_{tot} \cdot (\sum \frac{l_i}{A_i \cdot E_i})^{-1} \tag{3.10}$$

3.2.3 Numerical modelling

The numerical modelling was performed in Abaqus. Some simplifications were made. The support- and loading-pins were simulated by using boundary conditions and constraints. The specimen were designed without wire channels and with open ends. Abaqus do not use units: However, by using values with the following units mm, N and MPa the final stress values will be in MPa. The specimen consist of a single extrude of the sketch in Figure 3.6. It was extruded 60mm, half of the specimen length. Mechanical properties of PETG were assigned, Young's modulus of 1400MPa and a Poisson ratio of 0.4. These values were gathered from Prusa Polymers technical data sheet for PETG and Guessasma et al. (2019). To simulate the loading-pin were the top line at the center constrained as rigid and a reference point were attached to the center of this line so that a concentrated force could be applied. The support-pins were simulated by constraining a partitioned line 50mm from the center. This line were restricted from movement in the Z-direction and one endpoint were restricted from movement in the Y-direction. Symmetry over the YZ-plane along the X-axis were applied to the center surface. The forces from the loading pin were attached to the reference point on the center line. Post-tension were simplified as pressure on the opposite side of the center plane, the function of total force were used. Center post tension were applied over the whole end surface and bottom post tension were applied to the bottom half section. Mesh size of 0.4mm resulting in three elements across the thickness. Hex elements were used.

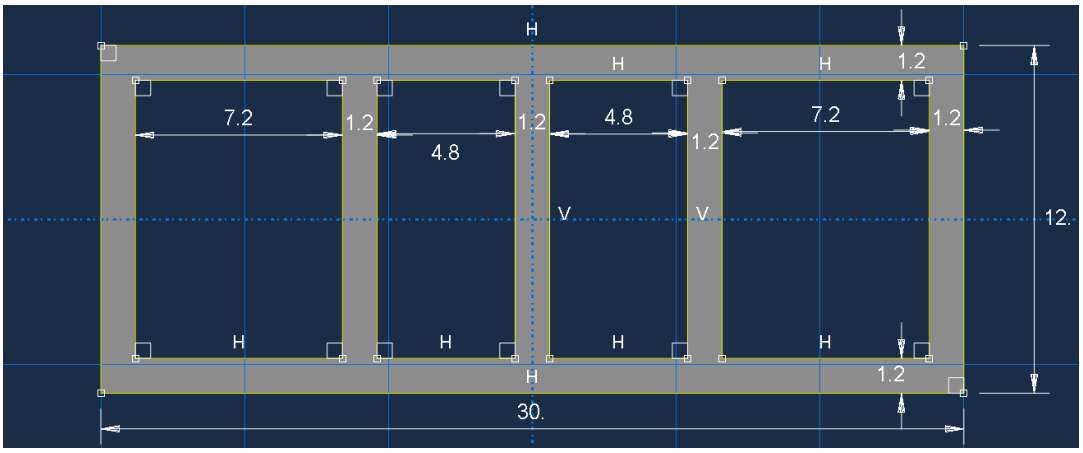

Figure 3.6: Sketch with dimensions of the extruded cross section in Abaqus. Remark: Distance between internal support walls are switched compared to printed specimen. Most likely this have negligible effect on simulated maximum stress results.

3.3 Phase C - Experimental testing

3.3.1 Static testing

The static 3-point bending tests were performed on a Chatillon CS2-1100. Support span was set to 100mm, supporting pins had a radius of 5mm and the loading pin had a radius of 9mm as seen in Figure 3.7. A loading-pin with a larger than typical radius is used to reduce the local stresses at contact point with the specimen. During testing the deflection of the loading-pin were set to 5 mm per minute, applied force and deflection were sampled 50 times every second. The data was then analysed in an Excel. Four different cases were tested, these will be referred to as C-C center control, B-C bottom control, C-PT center post-tension and B-PT bottom post-tension, as shown in Figure 3.5. For cases without post-tension were 8 tests performed, and for the cases with post-tension were 9 tests performed. One extra test were conducted on the post-tension specimens to observe internal deformation right after first load peak was reached.

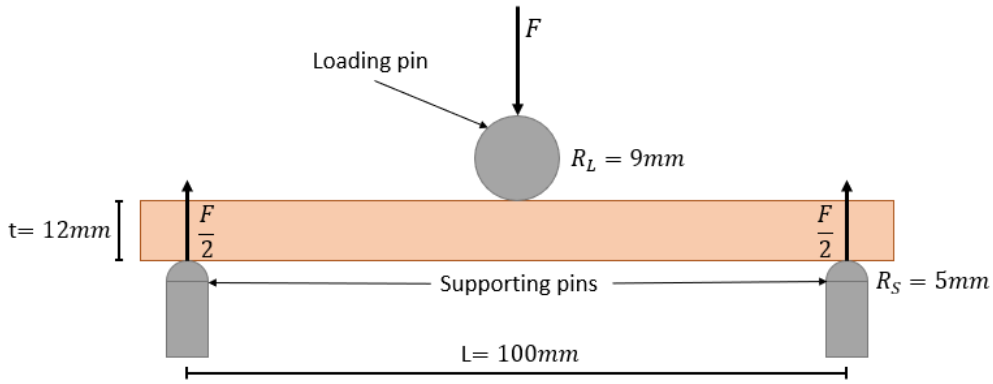

Figure 3.7: Three-point bending setup for static and fatigue tests.

3.3.2 Fatigue testing

The three-point fatigue tests were conducted on an Instron ElectroPuls E10000. The setup, dimensions and distances were equal to the static test. Specimens were subjected to a sinusoidal waveform loading with a stress ratio R=0.1. Tests were performed at 5 Hz. The same four cases as for static testing were performed in fatigue testing. Maximum fatigue load F_{max} were set to 76.3% and 66.8% of average maximum static load. A minimum of three specimen were tested for each case. If one of the values were significantly lower or higher than the others, an additional test was conducted. Test were stopped as the deflection reached 20mm.

3.3.3 Fractography

Microscopy analysis were done to investigate print quality and crack propagation. It was performed with a Hirox rH-2000 digital microscope with MXB-2500REZ lenses allowing for various magnifications up to 2500x. Fraction surface of samples from static and fatigue tests were analysed. The software allows for detailed capture of larger sections with automatic tiling. This function was only able to deliver high quality images of single layer fraction surfaces, as depth variations lead to unclear images. For this reason were there only made one image of a large section of a single layer fracture. This was of a static tested control specimen, Figure 4.17. All post-tension specimen had fracture surface divided over multiple layers and for this reason were only smaller sections captured.

Chapter 4

Results

4.1 Calculations and numerical modelling

4.1.1 Theoretical maximum three-point bending load

Calculations of maximum load were performed on the three different cross-section used in this thesis, specimen with wire channels in center, in bottom and without wire channels. These results gives a strength ratio between the different sections which can be used to compare the theoretical and experimental results. Maximum load and key values used in the calculations are listed in Table 4.1

Table 4.1: Values and results from calculating maximum theoretical strength of the different cross sections. (*) Ratio is the percentage difference from C-C F_{max}.

Type	C-C	B-C	X-C
σ_y (MPa)	30	30	30
I_y (mm^4)	2571	2581	2550
Center (mm)	6.00	5.90	6.00
F_{max} (N)	514.2	525.0	510.1
Ratio*	0.0%	2.1%	-0.8%

4.1.2 Post tension force

Based on the assumptions and formulas presented in 3.2.2 Compression force from post tension were theoretical compression force calculated for center and bottom post-tension specimen. This results in a theoretical applied force of: 2130.1N for center PT and 1775.0N for bottom PT.

4.1.3 Numerical modelling

The theoretical stress state can be found by performing numerical modelling. These stresses are linear dependent on loading-pin load and the compression loads from post tension. From this knowledge it is possible to create equations which give maximum stress based on these applied loads. The linear relationships between the loads and stress was created by isolating each of the loads and list the highest principal stresses as seen in Figure 4.1. An equation which give the exact same maximum value as the numerical model was then created. This was done by adding the stress equation from loading-pin load to the stress equation from center or bottom post tension, resulting in Equation 4.1 and Equation 4.2. To control the equation for center post tension, were the values compared to the theoretical value from force divided by area. By using the failure criteria of $\sigma_{max} = 30.0MPa$ from the material properties of PETG in Z-direction, can the maximum load without post tension be calculated to be 492.4N. The contour plot of this numerical model with the stress distribution can be seen in Figure 4.2, it can be observed that the maximum stress levels appear under the three internal vertical lines, the average stress in the bottom element row is in this case 28.4 MPa. For comparison reasons can the load at which the average stress is 30.0 MPa be calculated to be 520.3 N from the linear relationship between load and stress. The stress values of the different load cases and theoretical post tension force is listed in Table 4.2. The stress values are measured in the most critical element which is center element in the bottom row.

$$\sigma_{C.max} = 6.092 \cdot 10^{-2} \cdot F - 7.680 \cdot 10^{-3} \cdot P \tag{4.1}$$

$$\sigma_{B.max} = 6.092 \cdot 10^{-2} \cdot F - 1.646 \cdot 10^{-2} \cdot P \tag{4.2}$$

(F=Load on loading-pin, P=post tension force)

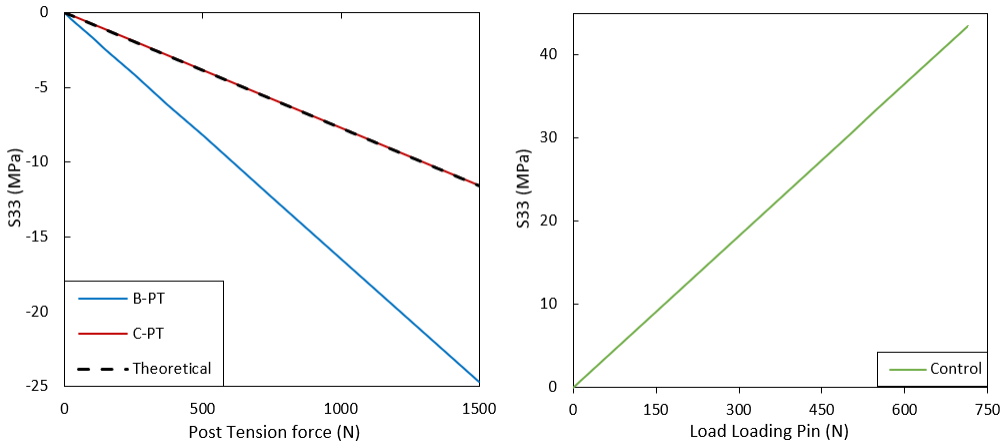

Figure 4.1: Linear relation between maximum stress along x-axis for post tension to the left and loading pin load to the right. S33 is equal to the principal stress in the bottom row of elements.

Table 4.2: Principal stress values in bottom center element from numerical modeling.

Type	**Principal stress (MPa)**	**PT load (N)**	**Loading pin (N)**
Center	-8.2	2130.1	0
Center	30.0	0	492.4
Center	30.0	2130.1	761.0
Bottom	-14.6	1775.0	0
Bottom	30.0	0	492.4
Bottom	30.0	1775.0	972.0

4.2 Experimental tests

4.2.1 Static tests

The maximum static load in 3-point bending are presented in Figure 4.3 and the load displacement curves are presented in Figure 4.6. The results show that C-C specimen on average can take 524N before failure and B-C 529N. By applying post tension, the average maximum load

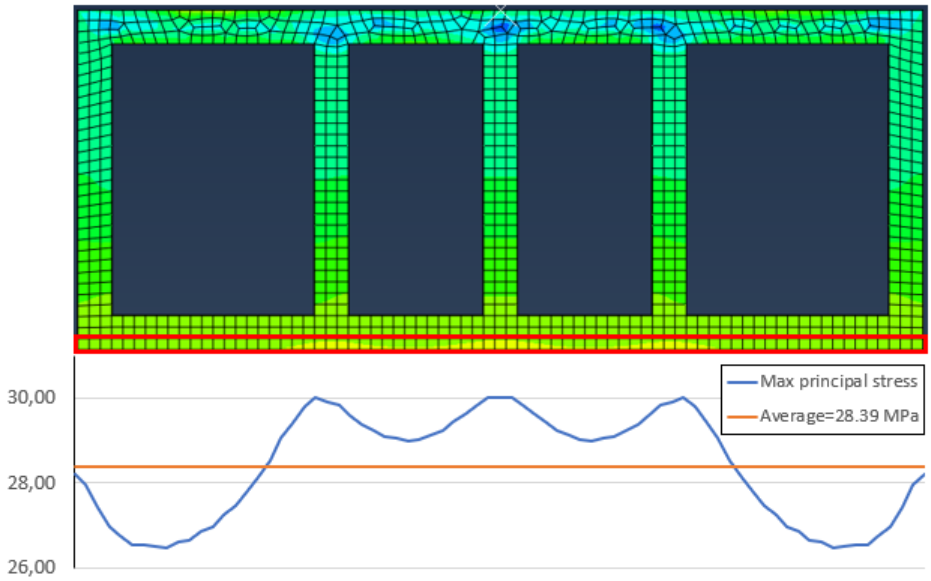

Figure 4.2: Numerical model of three-point bending without post tension. Contour plot of maximum principal stress in center cross section. Graph show stress distribution in bottom row of elements (marked in red) when loaded with 492.4N applied on loading pin. Orange line shows average stress.

increases with 5.6% for C-PT specimen and 34.8% for B-PT, labeled C-PT-1 and B-PT-1. Specimen with post tension achieve a second max load peak as one can see in the load-displacement graphs in figure 4.6, this average second load peak (C-PT2, B-PT2) has an average load of 251N for C and 455N for B. Compared to the control specimen is this a 52% reduction for C and 14% for B. The average load, standard deviation and maximum load from each testis listed in Table 4.3. There is a 9th test of C-PT and B-PT, these extra tests were performed to investigate if the wire channel was deformed after the first load peak and were stopped right after the crack initiation. The result from these two samples showed small marks from the wires, but no large deformations or cracks. One of the results from B-C was eliminated due to visual large defect on the crack surface, the average load is therefor based on seven test results. The PT tests were ran past second load peak and were stopped at a deflection of 10mm to 15mm for center specimen and 15mm to 20mm for bottom specimen. One sample of each of the post tension types were run past 25mm deflection to see how they behaved at larger deflections. All static post-tension tests were stopped by the operator as deformations got large, there was no complete failure of specimen or steel wire. Figure 4.4 and 4.5 shows load deflection curve of C-PT and B-PT samples

linked to crack propagation. These cracks propagates both vertically and horizontal, this was not the case for all post-tension specimen as the majority of the samples had cracks that grew mostly in the vertical axis. Figure 4.6 shows the majority of the load deflection curves. Some of the curves are not showed because a few of the files containing the load displacement data were lost. However, all the peak values were written down and presented are presented in Table 4.3. From the graphs one can see that all the PT samples have much higher toughness due to the higher maximum load and the ductile failure behavior after first load peak. The horizontal lines in the graphs are likely a result of stick–slip friction between the supporting pins and the specimen, and displacement-correction made made by the test machine due to the set condition of constant deflection of 5mm/min.

Table 4.3: Static test results from thee-point bending.

	Center (N)			**Bottom (N)**		
	Control	**PT 1**	**PT 2**	**Control**	**PT 1**	**PT 2**
Samples	515	578	270	541	687	480
	534	530	234	519	670	471
	449	561	268	520	718	449
	521	514	268	553	716	302
	607	494	267	548	726	503
	442	543	268	496	759	481
	642	575	296	528	745	446
	484	634	139	~~373~~	658	511
	-	625	-	-	742	-
Average	**524.3**	**553.6**	**251.3**	**529.3**	**713.4**	**455.4**
SD	**66.1**	**44.6**	**45.2**	**18.3**	**32.9**	**61.8**

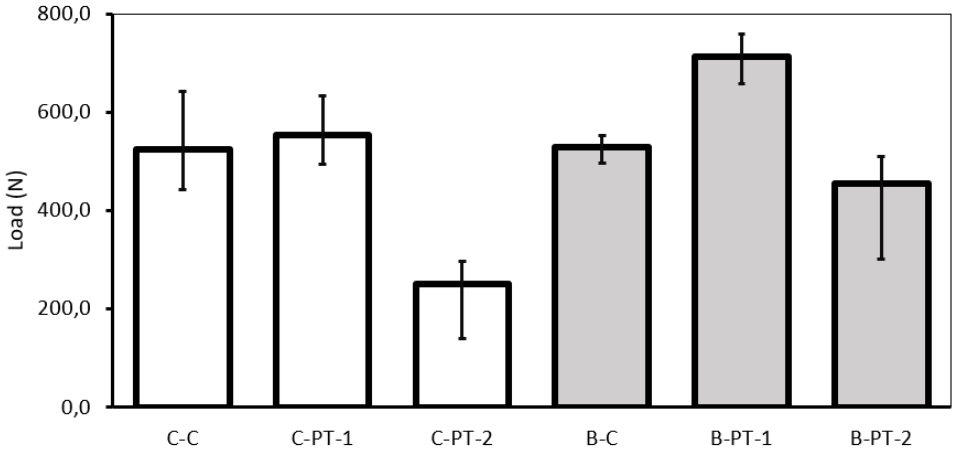

Figure 4.3: Average maximum load from static three-point bending test. Error bars indicates maximum and minimum values within each category.

Figure 4.6 shows a crack propagation related to deflection and force for C-PT. The initial crack appear off center due to a weak layer, then propagates towards the center as the load increases.

In both C-PT and B-PT one can observe a shift in the load-displacement curve, this is happens as the bottom of the specimen goes from a straight or concave shape to convex. In this section the post tension wire goes from being in contact with the lower section of the channel to the top section. In C-PT this appears in the section between 0N and 100N, in B-PT between 50N to 400N.

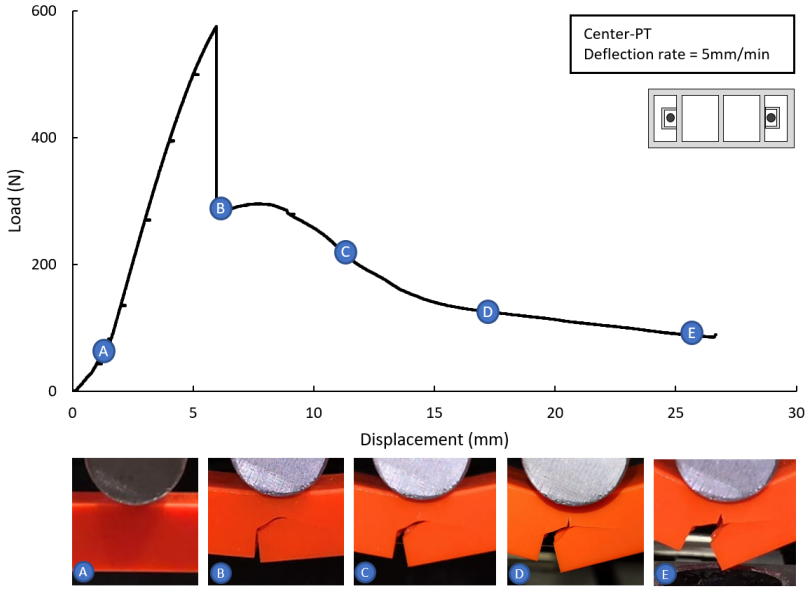

Figure 4.4: Load-displacement curve of static three-point bending test on C-PT specimen related to crack propagation.

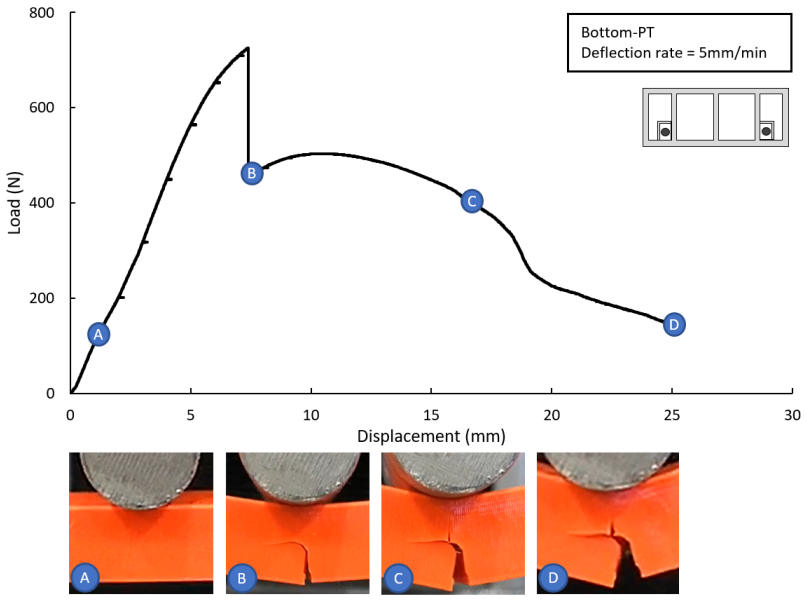

Figure 4.5: Load-displacement curve of static three-point bending test on B-PT specimen related to crack propagation.

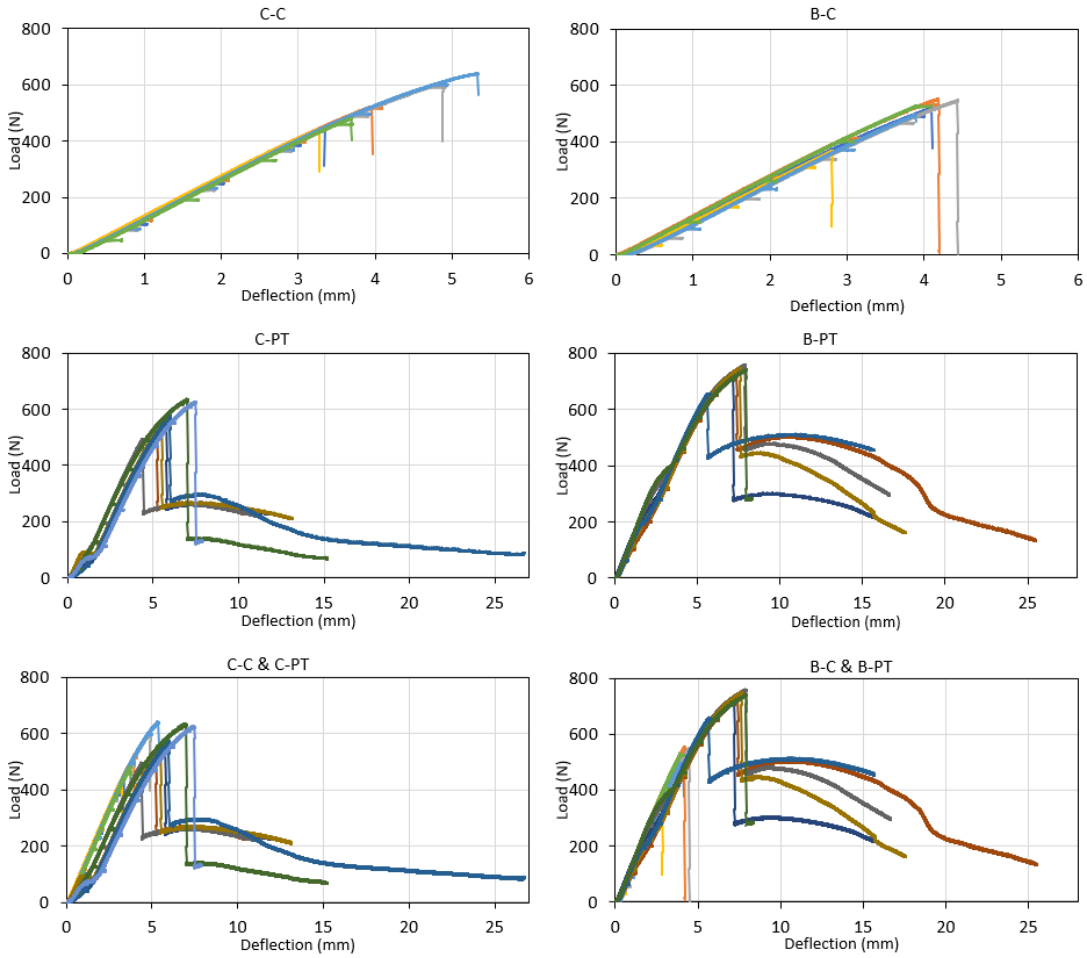

Figure 4.6: Load-displacement curves of static three-point bending tests of C-C, C-PT, B-C and B-PT specimen. Post tension samples were manually stopped due to large deflections.

4.2.2 Fatigue tests

Figure 4.7 shows the average fatigue life and the spread of the four different test groups at different load levels. Cycles are listed in a logarithmic scale. The error bars indicate the spread of the data, the standard deviation is listed as percentage of average fatigue life in parentheses. Samples counted as run out are marked with an arrow. Figure 4.8 shows the same data in one plot with normalized maximum load. The samples are loaded at 66.8% and 76.3% of average maximum static load except for two B-PT samples which were tested at lower loads to investigate the effect of crack appearance. The result shows significantly improved fatigue life in samples with post-tension with lower/less spread. Generally fatigue life increases as the load decreases as is expected. This is true for all cases except for C-C. However, this is likely due to low sample size and the large spread. There is a tendency that the error bar is larger on the lower end of the average. Run out result was only achieved among B-PT tests, the samples loaded at 476N, 400N and 350N were stopped as they reached 1M and 885k cycles.

Figure 4.9 show the relationships between cyclic deflection and cycles for each load case. Cyclic deflection is defined as the distance the load pin travels per cycle. For the control specimen and most of C-PT specimen the there is almost no change in cyclic deflection before failure. Some of the C-PT have a short gradually increase of cyclic displacement before failure. In the B-PT samples loaded at 476N and lower achieved run-out results, the cyclic displacement graphs shows some sudden changes.

Figure 4.11 show image correlations were the large changes in cyclic deflections can be linked to crack initiations and crack propagation. In B-PT loaded at 350N no visual cracks appeared during the 885k cycles and no large changes in cyclic deflection was observed, indicating that endurance limit is reached. In B-PT loaded at 400N started crack initiation at around 94k cycles according to the graph, it gradually propagates until it stabilizes around 110k. For B-PT loaded at 476N were crack initiated at around 28k cycles, with most rapid growth for the first approximate 10k cycles, then slow growth for the next 100k cycles. Crack propagation of the reminding 850k cycles were approximately 1.5mm, as seen in Figure 4.11.

Figure 4.12 shows cyclic deflection related to crack propagation, it were observed that crack

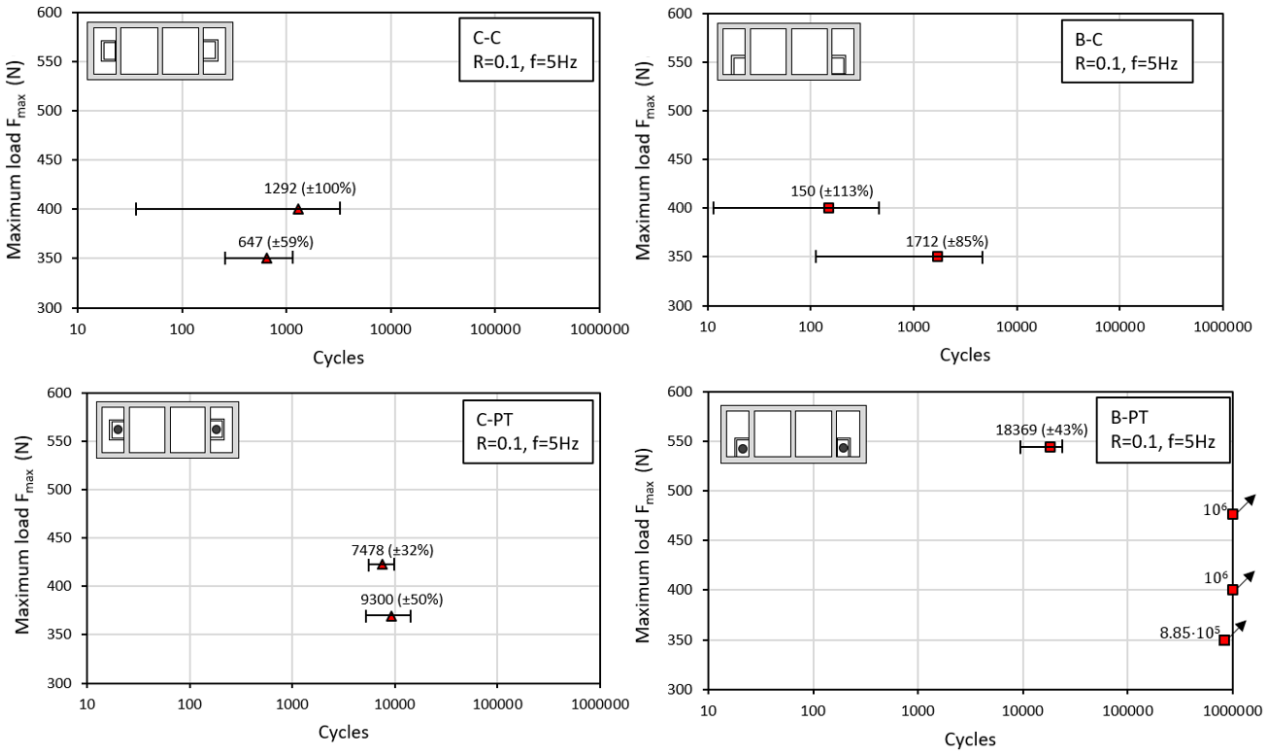

Figure 4.7: Fatigue life related to maximum fatigue load, error bar shows spread of result within each case values in parentheses is standard deviation in percentage of average fatigue life. Arrows indicate run out samples.

initiation in this case happens around 700 cycles before failure. Fracture happened off center, indicating a weak layer.

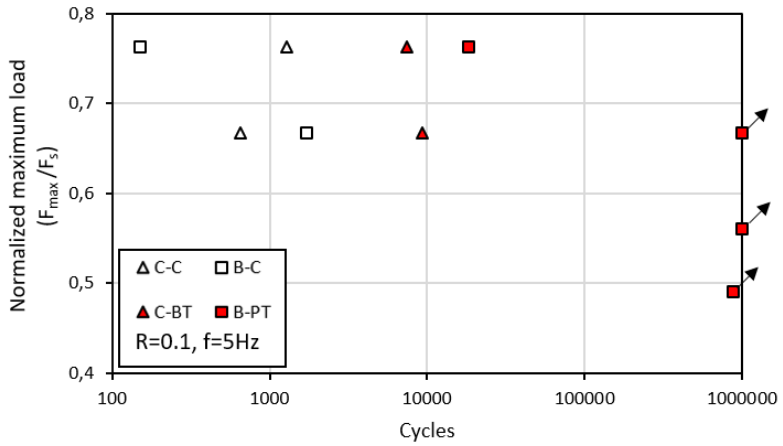

Figure 4.8: Average fatigue life related to normalized maximum fatigue load of all cases. Arrows indicate run out samples.

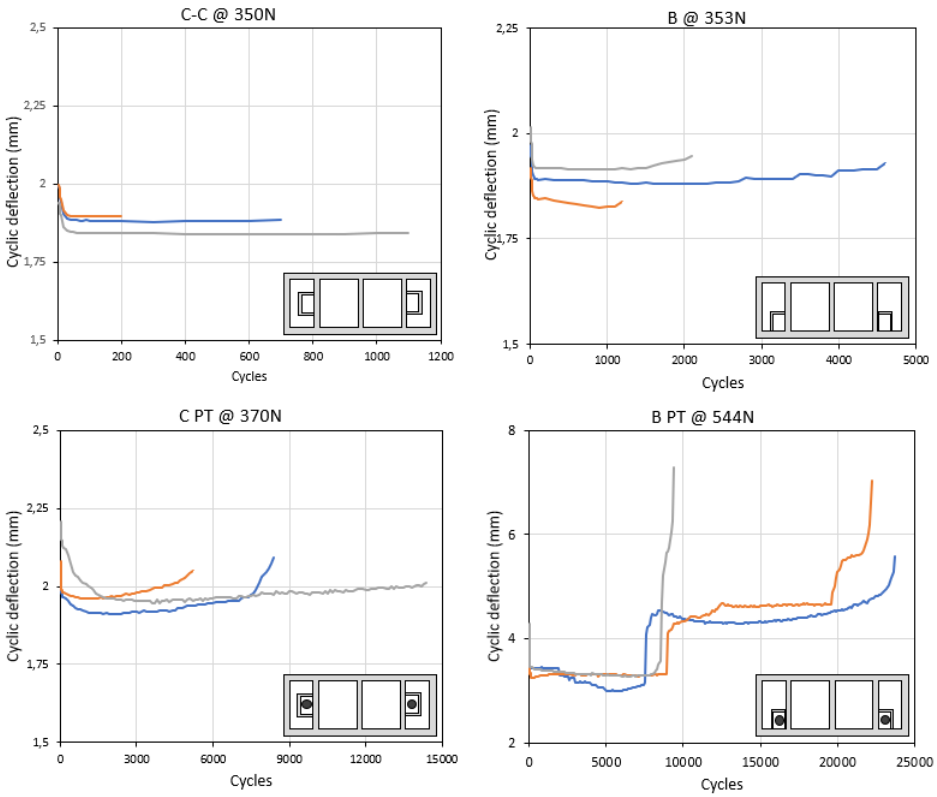

Figure 4.9: Cyclic displacement at loading-point of specimen related to number of cycles. One of each case were selected as they show the tendency within that group.

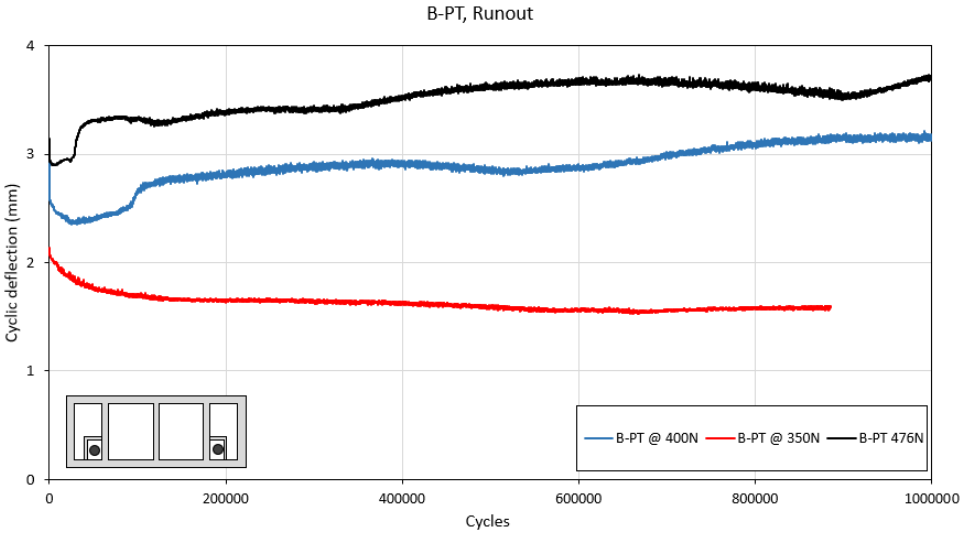

Figure 4.10: Load-displacement curves of static three-point bending tests of runout B-PT samples.

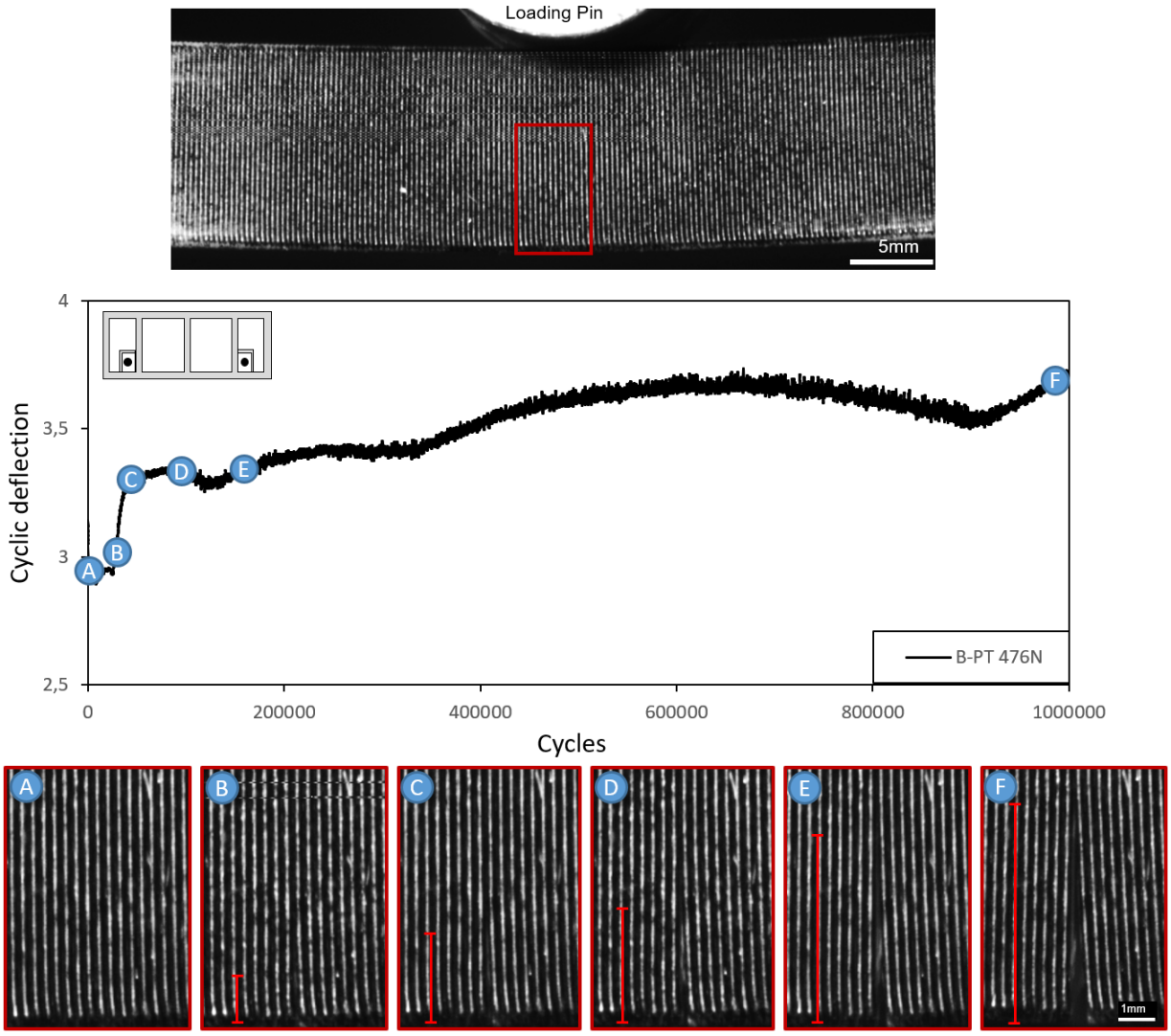

Figure 4.11: Cyclic displacement of a bottom post tension specimen linked to images of crack propagation. R=0.1, 5Hz, maximum load 476N, stopped after 1M cycles.

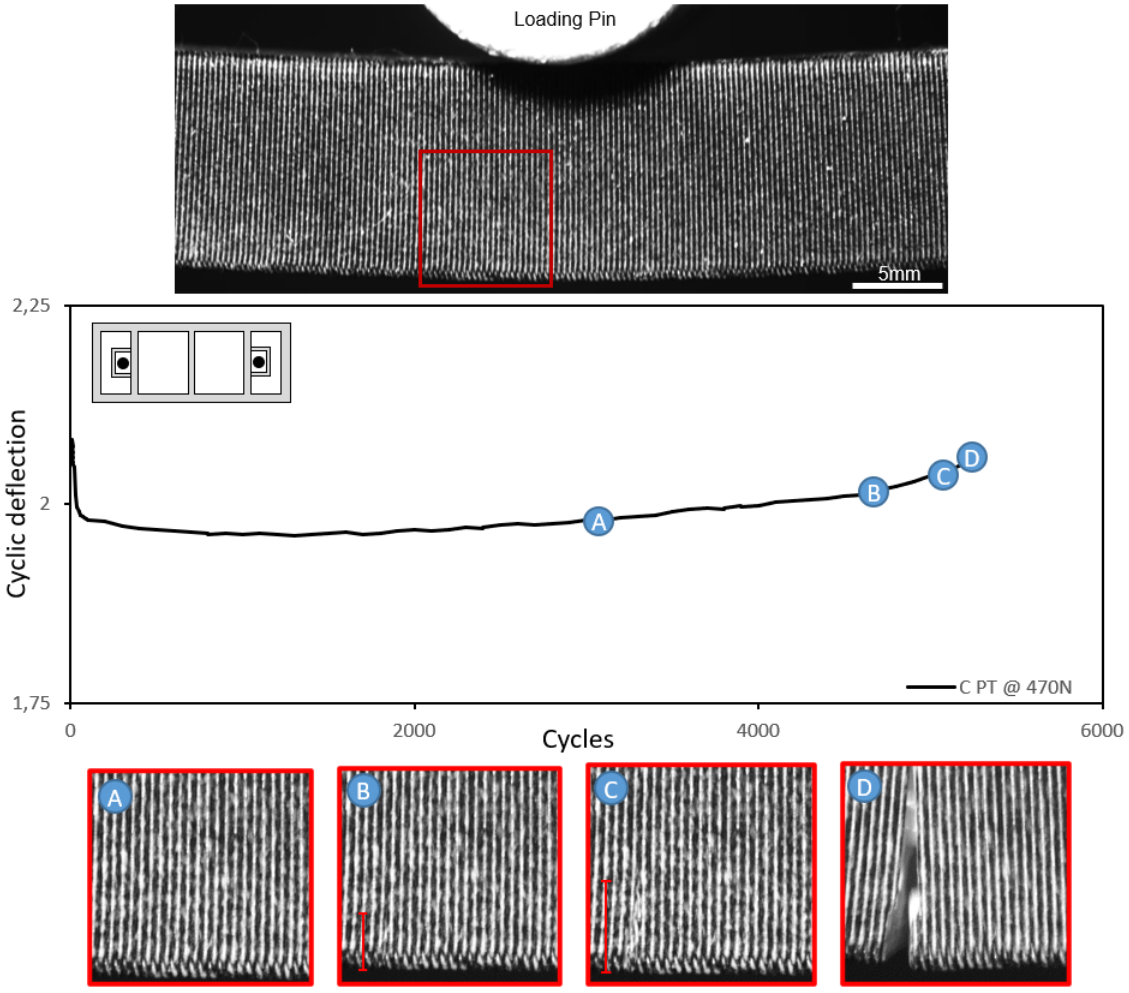

Figure 4.12: Cyclic displacement of a center post-tension specimen linked to images of crack propagation, R=0.1, 5Hz, maximum load 470N, failure after 5186 cycles.

4.3 Fractography

Microscopy images shows large defects in the structure of specimen, some are shown in Figure 4.13-4.16. The defects are mainly in the form of voids, incomplete fusion and air bubbles, these type of defects are found throughout the cross section. The concentration of defects are larger in the tee-sections, where the horizontal and vertical lines meet. This is due to start and stop in the deposition process and lack of material in sharp corners. Figure 4.14 shows a cross section of the sidewall of the specimen. Continuous voids in the printing direction can be seen between the printed filament. The cracks along the voids was a result of the cutting procedure. Rib-marks can clearly be seen moving from left to right in the direction of the cut. Similar voids, as in Figure 4.14 is shown in Figure 4.16. It shows that the cross section area of the fusion zone is much smaller than the center of the layer.

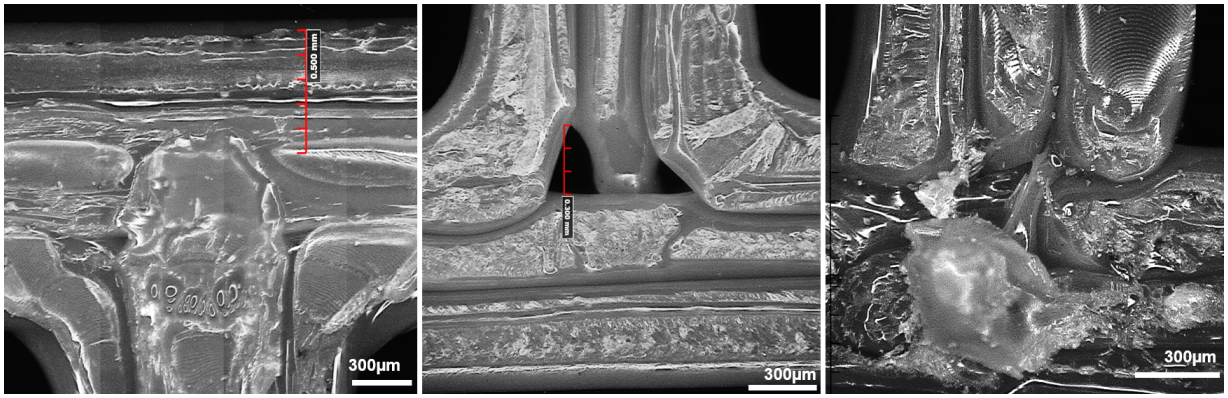

Figure 4.13: Left: Top T-joints with micro bubbles. Center: Bottom T-joint with two continuous voids in the build direction. Right: Bottom T-joint with voids lack of fusion, rib-marks indicating that a crack has initiated from the void.

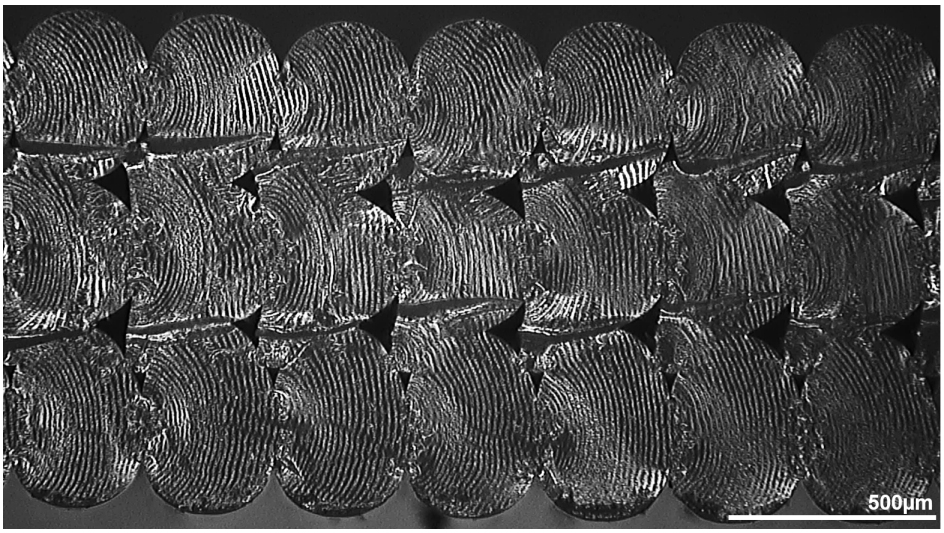

Figure 4.14: Image taken parallel to deposition direction showing continuous voids. Cut made by knife resulting in a rib-marks on the fracture surface propagating from left to right. The cutting process also caused the fractures between the voids.

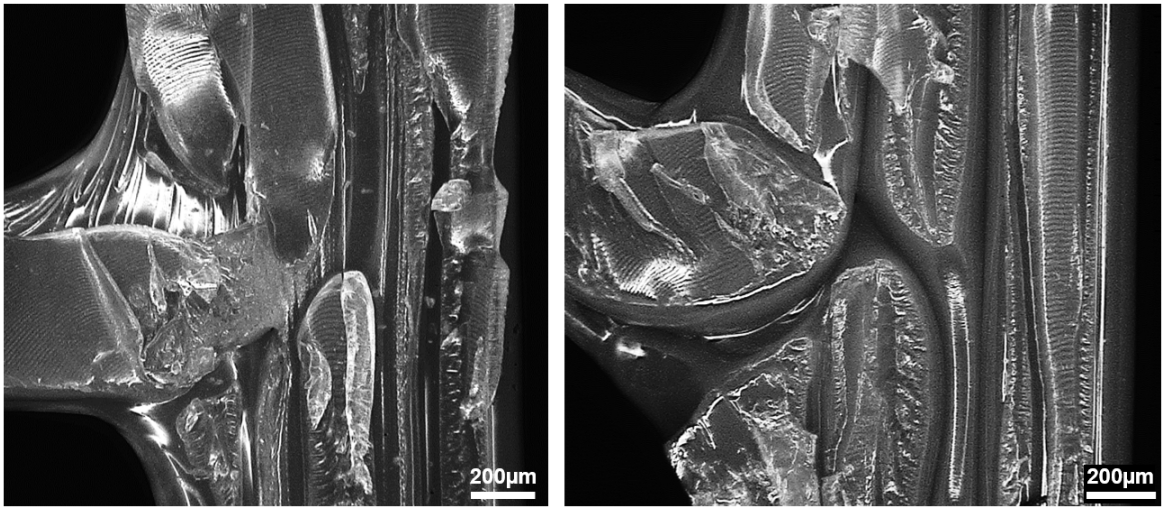

Figure 4.15: Joint between vertical support and wire channel, both images shows sections with lack of fusion, voids and rib-marks.

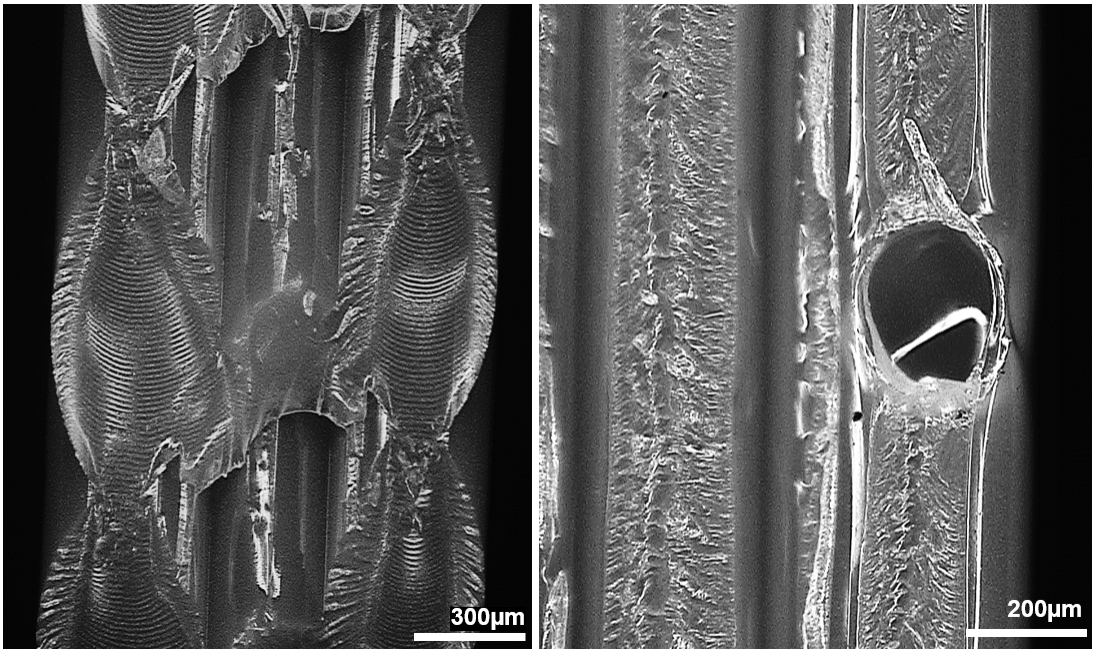

Figure 4.16: Left: Crack propagation across layers showing large continues voids between layers and reduced fusion area between layers. Right: Large gas bubble in deposited filament.

Large continuous voids normal to the printing plane was observed in some of the tee-sections as in the center image in Figure 4.13, the left image is of a top tee-section showing some micro bubbles, right image is of a large zone of poor fusion in a bottom tee-section. It was observed that the bottom section had a much rougher surface than the top section. Figure 4.15 shows the tee-section were vertical lines and the wall of the wire channels meets, this zone is also full of voids and poor fusion. The left image in Figure 4.16 shows the fracture surface of a crack that have propagated across multiple layers, the reduced effective cross-sectional area between layers is well illustrated. The right image shows a large gas bubble.

In most of the microscopy figures one can observe rib-marks. These were present in all the analysed samples both static and fatigue. The largest concentration of rib-marks were observed in the top section where the force from the loading pin was applied. There was observed a tendency that the concentration of rib-marks was reduced as the distance from the top increased. There were also a tendency that in B-PT samples the rib-marks were observed further away from the top section. Rib-marks were significantly more present among C-C and B-C specimen, then

C-PT specimen and least present in B-PT specimen. Figure 4.17 shows a large section of a C-C fracture surface from a static test. One can see that the majority of the rib-marks in the vertical sections have the concave side facing downwards, meaning that the fracture has propagated upwards. In general it was observed that there was a tendency that the fracture origin were located somewhere in the tee-section. Among the fatigue samples there were found sections of striations in the B-PT samples like the ones observed in figure 4.20, which seems to be from fatigue. However, few samples were investigated that closely. Although long sections of rib-marks were less common in B-PT some were observed as seen in in Figure 4.18, rib-marks were not found this low C-C, B-C or C-PT.

Figure 4.17: Large section of center specimen fracture surface after static test. Center images shows rib-marks, crack growth direction is illustrated with arrows. (Rib-marks are not due to fatigue).

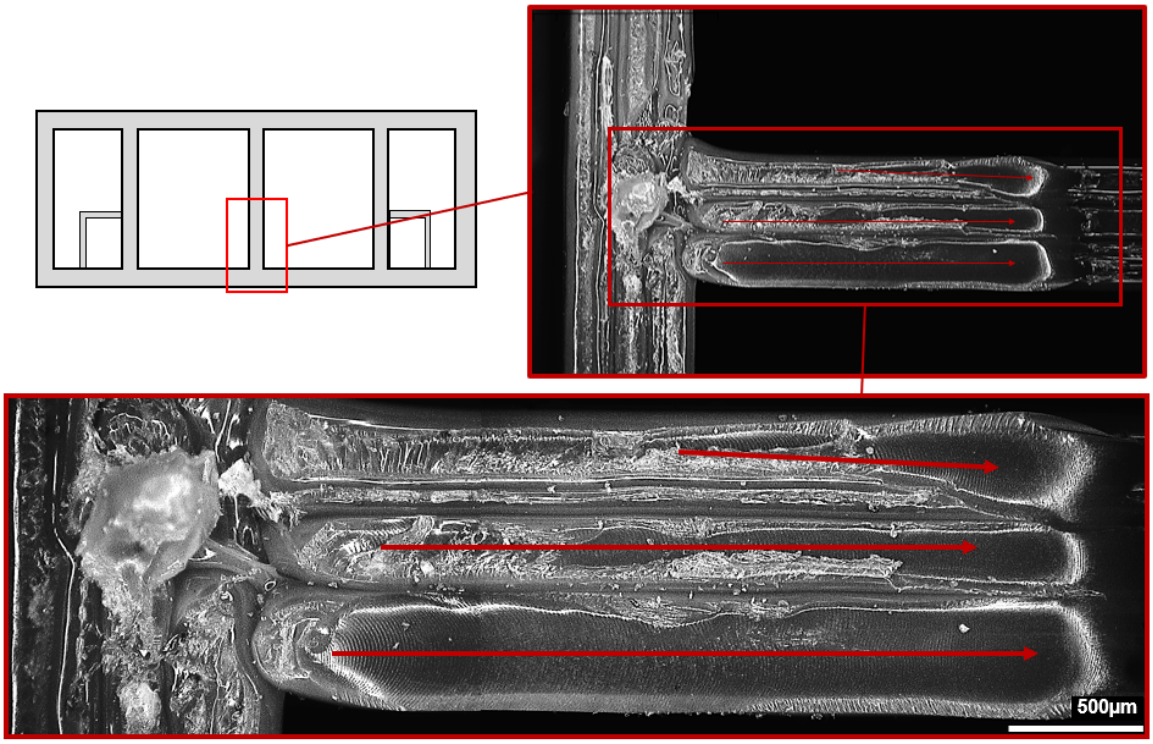

Figure 4.18: Fracture surface from fatigue B-PT sample. Images are rotated 90°. Shows crack initiation and growth direction. Fracture marks are thought to be rib-marks and not fatigue striations as they are not distinguishable from marks observed in static tests.

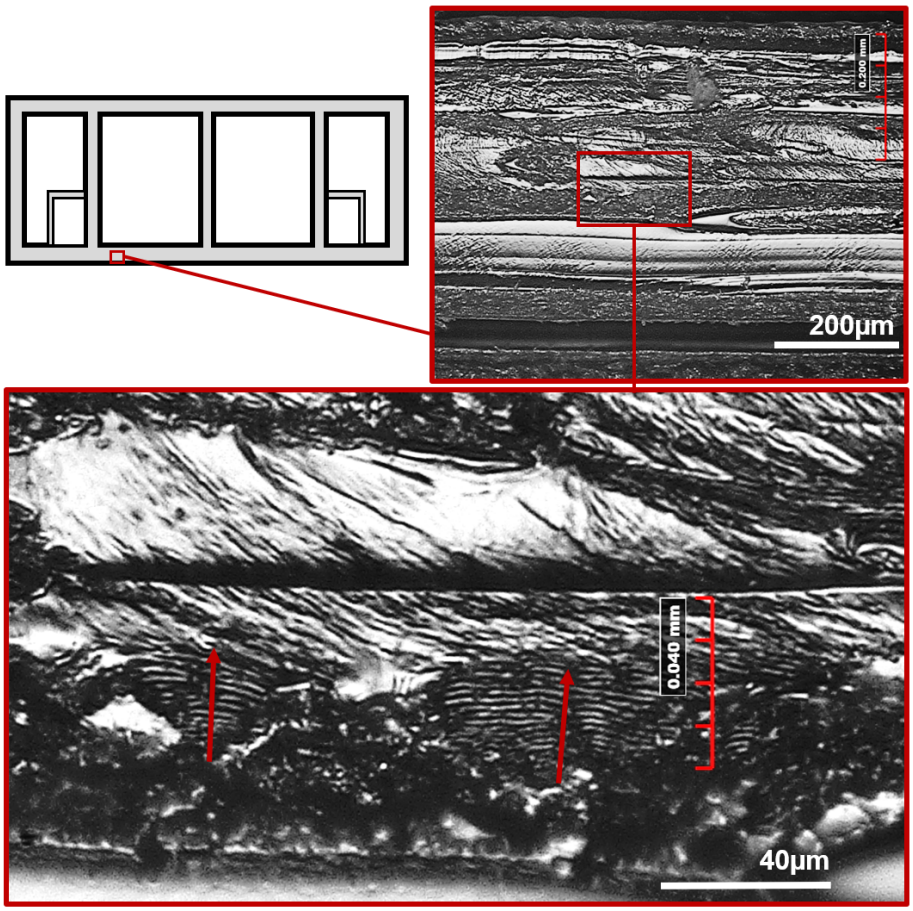

Figure 4.19: Fracture surface of fatigue B-PT sample. Images shows fatigue striations in the bottom section of the specimen.

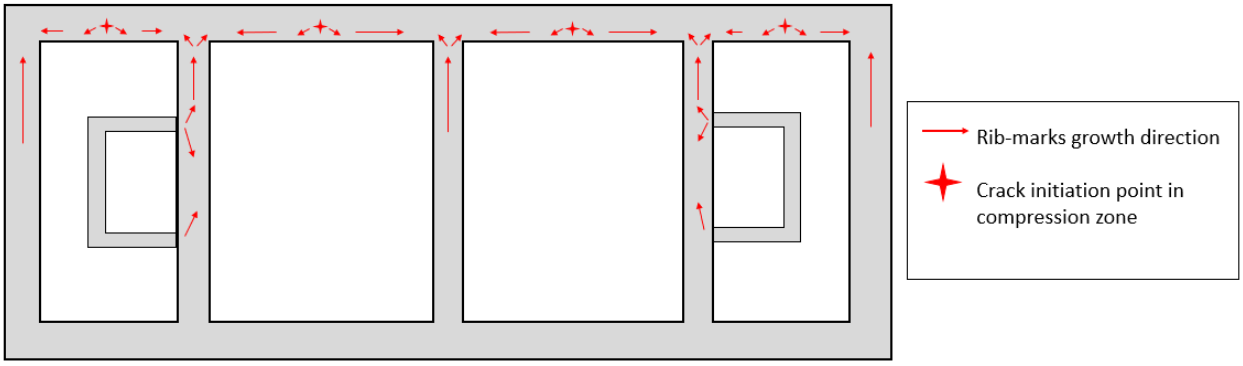

Figure 4.20: Illustration shows the general crack growth direction based on rib-marks and crack initiation in fracture surface. Illustration made based on observation done on static and fatigue fracture surfaces. Crack leading to failure grows from bottom and up without forming rib-marks.

Chapter 5

Discussion

5.1 Specimen and post-tension design

The structural cross section design of the specimen design was based on a hollow rectangle with three vertical walls. This made the specimens strong enough for testing with post-tension without deformation in the contact point of the loading-pin.

The selected number of vertical walls and their thickness, was balanced between strength and print time. The geometry was simple so that theoretical calculation and numerical modeling would be easier to conduct. Rectangular channels for the post-tension wires were added to the side of two of the walls and placed either in the center or the bottom. The purpose of the wire channels are to guide the wires when mounting the post tension system and to hold the wires in place during testing. The channels were made larger (2.5 x 3.5 mm) than the steel wires (d=1.2mm), this made the mounting process of the wires fast and simple regardless of the condition of the wire end section.

It was observed during the first tests that the wires moved slightly in the channels during testing, leading to less optimal placement of the wires.

Based on initial tests it was observed that wire movements and thin channel walls (0.4mm) had minor effect on the post tension experiments. It was decided to proceed with the current design, as it made it possible to perform reliable three-point bending tests that documented the

effect of using post-tension.

.

5.2 Print quality

The print quality may be evaluated by comparing maximum theoretical load, with average maximum experimental static loads. The theoretical load is based on the mechanical properties provided by the filament manufacturer(Prusa Polymers). These show that theoretical maximum load for C-C and B-C was 514.2N and 525.0N, and the experimental results were 524.3N and 529.3N. This is an increase of 2.0% and 1.0% relative to the theoretical values. The average increase of 1.5% are used in further calculations. There is a linear relation between load and stress, one can therefor state that experimental ultimate tensile stress is $1.015 \cdot 30MPa = 30.45MPa$.

However, since the stress values used in the theoretical calculations are obtained by tensile tests they are not directly comparable with the tensile stress values obtained from the experimental bending tests in this work (as stated in Chapter 2.2 Bending and tensile strength).

Assuming that the ratio between maximum tensile stress and maximum bending stress is equal for PLA and PETG one can use the ratio of the values from Chacón et al. (2017). This article documents that maximum tensile stress obtained in specimen is 28% lower in tensile tests than in three-point bending tests, due to the larger critical volume in tensile test.

By using this ratio one can state that actual comparable tensile strength of the experimental specimen is around $30.45 \cdot 0.72 = 21.9MPa$. This is lower than the tensile strength range given by Prusa which is 30±5 MPa. The estimate of a tensile strength of 21.9 MPa is a rough estimate, but it indicates material strength of the material used in this work is in the lower strength range. This is likely due to the fact that standard printing parameters with increased layer thickness were selected, and not parameters optimized for strength as in the Prusa tests.

By comparing the printer parameters in Table 3.1 and using the theory in Chapter 2.1.4 one can assume that the difference in strength between the specimen used to obtain the strength values in Prusa Polymers PETG data sheet and this experiment is due to multiple printer param-

eters that are better for strength. Prusa experiment uses a higher nozzle temperature increasing time over T_g improving bonds strength. They were made with increased extrusion multiplier of 1.07, meaning a 7% increase in material flow resulting in more material, smaller voids and higher strengths. Even though the Prusa samples were printed using the FAST setting, with infill speed reduced from 200mm/s to 100mm/s making it only slightly faster than the 80mm/s in QUALITY setting used in the specimen used in this research. Faster printing times leads to less cooling of previous layer, hence increasing fusion between layers. The less optimal printer parameters likely caused the material to be weaker than the material properties given by the filament manufacturer. However, this reduction caused the obtained experimental bending strength to match the listed tensile strength used for theoretical calculations, hence making the experimental and theoretical results more comparable.

5.3 Static test results

In this section is the static strength with and without post tension compared and discussed. The values from Chapter 4 of maximum theoretical and experimental three-point bending loads are listed in Table 5.1.

Table 5.1: Maximum failure load based on a theoretical failure stress in Z-direction of 30 MPa and experimental results

Type	C-C	B-C	C-PT	B-PT
Theoretical calculations (N)	514.2	525.0	-	-
Numerical modeling (N)	492.4	492.4	761.0	972.0
Experimental (N)	524.3	529.3	553.6	713.4

5.3.1 Control

The maximum load values shows a good correlation between theoretical and experimental results on the specimens without post tension. Numerical modeling results are slightly lower than the results from theoretical calculations, this is likely because they are based the most critical element. If the average value of the bottom element row is used instead of the most critical

element the maximum load is 520.3 N, which is between C-C and B-C results from theoretical calculations. The theoretical calculations performed on the cross section without wire channels resulted in a maximum load of 510.1N. It was expected that the results from the numerical model would be similar, as their cross section were equal. The 2.0% difference between the two could be because of too large elements in the numerical model or because of the geometry of the cross section which lead to variable stress levels across the bottom section of the specimen.

As stated in Chapter 5.2 is the good correlation between theoretical and experimental strength values likely a coincidence, for the reason that the obtained bending strength of the specimens is close to the tensile strength presented in the PETG technical data sheet, which was used in theoretical calculations and the numerical models. The good correlation in static results increases the validity the part of the equations from the numerical models related to stress from the loading-pin.

5.3.2 Post-tension

Post-tension results are more difficult to predict with theoretical calculation or a numerical model, as the setup is more complex than the control specimen. The theoretical post-tension strength from the numerical models are higher than the experimental results, 37.5% for C-PT and 36.2% for B-PT. By just analysing these values it might look like there is just a factor that is wrong. However, by comparing the post-tension results to the theoretical and experimental results without post-tension it becomes clear that the numerical post-tension model overestimate the strength gained from post-tension. The numerical model shows an increase due to post-tension in center of 54.5% and 97.4% for bottom. The equivalent experimental results are 5.6% and 34.8%. For this reason it can be stated that the numerical model do not correspond well to the real test results.

The large difference between the theoretical and the experimental results can be due to the assumptions and simplifications done in the numerical model or that the assumed failure mechanism is wrong and that there is other factors contributing to the failure other than maximum principal stress in the bottom section.

In advance of the testing it was assumed that the numerical model would result in lower maximum loads than the experimental results. This was because of the assumptions that were made. Especially the assumptions that finger pre-tightening of the nuts leads to a neutral stress state and that there would be no deflection in the specimen. The finger pre-tightening was performed until the moment were too large for fingers to tightening further, hence were some tension applied to the wires before the wrench was used. Meaning that the assumption of neutral stress state in the wires after finger pre-tightening were not accurate and that the actual tension were slightly higher. The assumption that there were no deflection in the specimen is relative accurate for C-PT as it stays relatively straight as post-tension is applied, during testing the wires are held in the neutral axis which do not lead to change in the wire stress, as the length of the neutral axis stays constant during bending. For B-PT is the assumption less correct. The specimen is bent as post-tension is applied in the bottom section, leading to less stress in the wire and less compression force from the post tension system. During three-point bending the specimen is bent the opposite direction leading to higher stress and compression force than calculated.

For these reasons were it expected that using external pressure for the post-tension system were a reasonable simplification for the C-PT model. And that these results would correspond better to experimental results than for B-PT. However, both results are almost equally far from experimental results.

The fact that the actual compression force from the post-tension likely is higher than in the numerical model, and that the experimental results still are much lower than numerical results, indicates that the the failure load can not simply be calculated by using the superposition principle with stresses from post-tension and bending moment.

Fractography and inspection was performed in an attempt to inspect if localized stress increase due to contact with the post tension wires or loading pin, could cause failure. By inspecting the wire channels after first load-peak small marks from the wire were observed, but no deformation or cracks linked to the wire channels. Hence this neither validate or falsify its contribution to failure. Microscope images shows rib-marks which in some cases originates

from the wire-channels. This was observed in both specimens with and without post-tension, indicating that it is a result of defects from the printing process, not stress from the post-tension wires.

The microscope images also showed rib-marks in the top section of all the inspected fracture surfaces, the markings are thought to be a result of the local stresses from contact with the loading-pin. These marks are more present in specimens without post-tension and can therefor not explain why post-tension specimen perform worse than calculated, while control specimen calculations are relatively accurate.

The reason why average maximum load of C-PT is only 5.6% higher than C-C, when it in theory should be approximately 50% higher, is not fully understood. Experimental results of B-PT did also perform worse than calculated, but showed strength increase of 34.8%. Regardless of improvement in static strength does post tension in both center and bottom provide benefits by increased predictability and more desirable failure characteristic, which is changed from brittle to semi-brittle. This results in increased toughness and possible early warning before total failure.

Post script: Real shortening of centre post-tensioned specimen were measured to be 1.15mm where as used calculated shortening was 1.344mm. Meaning that the real compression force from center post-tension is around 14% less than what is used in calculations, hence should P in Equation 4.1 be multiplied with 0.86. The difference is still not significant enough to explain the large difference between calculated results based on the numerical model and the experimental results for center post-tension. Measure the shortening of bottom-post tensioned specimen was unfeasible due to the deflections.

5.4 Fatigue test results

The fatigue test were conducted with with the same three-point bending setup as the static test. Specimens were loaded with a fatigue stress ratio R=0.1 at a rate of 5Hz. To have the results more

comparable were the loads set to equal normalized values based on average maximum static load. All cases were tested at 0.763 or 0.668 of maximum static load, with two B-PT samples that were tested at 0.561 and 0.491 to investigate fatigue behavior at lower relative load. Average values for each case is listed in Table 5.2.

Table 5.2: Average fatigue life for the different load cases.Normalized load is maximum fatigue load divided by maximum static failure load. (*) runout with crack, (**) runout without crack.

Normalized load	C-C	B-C	C-PT	B-PT
0.763	1292	150	7478	18369
0.668	647	1712	9300	1000000*
0.561	-	-	-	1000000*
0.491	-	-	-	885000**

5.4.1 Control

The fatigue tests performed on the control group highlights the weakness of FFF components at cyclic loading(Figure 4.7). The results shows a very large spread within each group, the standard deviation being between 59% and 113% of average value. Within most groups there is results in the range from around 100 cycles up to a few thousands.

It is expected in fatigue testing that fatigue life significantly increases as the load decreases. This is the case for B-C samples which get an average increase of around 10 times as many cycles when the max cyclic load is decreased from 400N to 350N. For C-C the average fatigue life doubles as the load is increased, which is opposite of what one would expect.

Based on the relative similar geometry one would assume that C-C and B-C would have similar results loaded at approximately the same loads. But C-C loaded at 400N(76.3%) have an average of 1292 cycles and B-C loaded at 404N(76.3%) has an average of 150 cycles. At 350N(66.8%) and 353N(66.8%) are the values 647 cycles for C-C and 1712 cycles for B-C. The large variation of average cycles loaded at approximately the same load is likely a result of the low sample size of 3-4, resulting in the large spread of the data. By looking at figure 4.7 one can see that the average number of cycles is on the upper half of the data spread. This indicates that there is a larger possibility of outlier values at the lower end of the spectrum, likely because of larger defects. One

could argue that specimen with very low fatigue life should be disqualified and removed from the results due to these defects. However, since one can not simply know if these kind of defects are present before testing it would not show the full picture. Another argument to use all the data is that non of the post-tension specimen failed before 5000 cycles, were as several of the control specimen failed below 100 cycles. Hence is it likely that post-tension reduce the critical effect of defects in FFF parts. It would therefor be favorable to just remove data from the control data sets.

5.4.2 Post-tension

The improvement in static strength with post-tension in center were low with an increased strength of 5.6%. In fatigue are the results better. Test results shows that center post-tension specimen got a 5.8 to 14.4 times increase in fatigue life compared to the control group when loaded at 76.3% and 66.8% of maximum static load. Relative standard deviation is also improved with a reduction from 100% and 59% to 32% and 50%. Showing that post-tension in center contributes to more predictable and significantly higher fatigue life.

Results from fatigue test of B-PT are better results, with 2.5 as many cycles than C-PT when loaded at 76.3% of maximum static load and run-out results for all specimen loaded at 66.8% or lower. Crack initiation occur in the specimens loaded at 476N (66.8%) and 400N (56.1%) after 28k and 94k cycles. Based on cyclic deflection curves and image correlation of crack growth is it shown that the crack growth were largest right after crack initiation(4.11). For the specimen loaded at 476N did the majority of the crack growth take place during the first 100k cycles after crack initiation, before the it stabilized. This is likely a result of the steel wires taking more of the load as the crack propagates. The steel wires take more of the load because the effective neutral axis moves upwards as the crack grows, hence increasing the steel wires strength contribution.

The B-PT fatigue test performed at 350N(49.1%) resulted in runout and no visual cracks. Cyclic deflection curve in Figure 4.10 has no sudden changes and supports the visual inspection that no crack or plastic deformation have taken place in this specimen. Being able to withstand 885k cycles without any sign of weakening indicates that endurance limit possibly has been

reached. For reference did B-C loaded at 353N fail on average after 1712 cycles, emphasising the potential the potential post-tension has in cyclic loading.

Chapter 6

Conclusion

This research aimed to document the the effect post tension has on Z-strength in parts made by FFF. Based on the experimental results from static and fatigue three-point bending tests improved strength, predictability, toughness and failure characteristic documented. The results from static test shows good correlation between experimental and theoretical values for specimen without post-tension. However, the same comparison with post-tension shows less improvement than the numerical model predict. Especially the strength increase from post-tension in the neutral axis (center) was lower than expected, with an average increase in maximum static load of 5.6%. Post-tension placed in the bottom section of the specimen resulted in an average increase of 34.8% for maximum static load.

Fatigue tests of the control specimens showed large variation in results. For center post-tension specimen loaded at the same normalized loads the number of cycles to failure increased by a factor of 5.8 to 14.4, and relative standard deviation was approximately reduced by 50%. Bottom post-tension specimen loaded at the highest normalized load (76.3%) were further increased by a factor of 2.5 compared with center post-tension specimen. Those loaded at 66.8% of maximum static load or lower achieved runout results, meaning that the test was stopped after 1 million cycles. These had cracks which were held held together by the post-tension system.

The specimen loaded at 49.1% of maximum static load were stopped after 885k cycles without any signs of cracks or deformations, indicating that the endurance limit might have been

reached. Specimen without post tension loaded at the same load had an average fatigue life of 1.7k.

The absence of outlier values among the post-tension results shows that post-tension reduces the effect defects has on especially fatigue life. The increase in strength, predictability and fatigue life may allow for post-tension FFF to be used in a wider range of applications.

To better understand and optimize the effect of post-tension further research may look into creating a more accurate numerical model, the effect of various levels of applied tension and the effect of applying post-tension in other print orientations.

The results from this research documents that post-tension can be used as a mechanical solution to improve the Z-strength in parts made by FFF.

Bibliography

Chacón, J., Caminero, M., García-Plaza, E., & Núñez, P. (2017). *Additive manufacturing of pla structures using fused deposition modelling: Effect of process parameters on mechanical properties and their optimal selection. Materials Design, 124*, 143–157. URL: https://www.sciencedirect.com/science/article/pii/S0264127517303143. doi:https://doi.org/10.1016/j.matdes.2017.03.065.

Céline Bellehumeur, Q. S. P. G., Longmei Li (2004). *Modeling of bond formation between polymer filaments in the fused deposition modeling process. Journal of Manufacturing Processes, 6*, 170–178. URL: https://www.sciencedirect.com/science/article/pii/S1526612504700717. doi:https://doi.org/10.1016/S1526-6125(04)70071-7.

Ferretti, P., Leon-Cardenas, C., Santi, G. M., Sali, M., Ciotti, E., Frizziero, L., Donnici, G., & Liverani, A. (2021). *Relationship between fdm 3d printing parameters study: Parameter optimization for lower defects. Polymers, 13*. URL: https://www.mdpi.com/2073-4360/13/13/2190. doi:10.3390/polym13132190.

Guessasma, S., Belhabib, S., & Nouri, H. (2019). *Printability and tensile performance of 3d printed polyethylene terephthalate glycol using fused deposition modelling. Polymers, 11*. URL: https://www.mdpi.com/2073-4360/11/7/1220. doi:10.3390/polym11071220.

Hayes, M. D., Edwards, D. B., & Shah, A. R. (2015). *4 - fractography basics.* In M. D. Hayes, D. B. Edwards, & A. R. Shah (Eds.), *Fractography in Failure Analysis of Polymers* Plastics Design Library (pp. 48–92). Oxford: William Andrew Publishing. URL: https://www.

sciencedirect.com/science/article/pii/B9780323242721000040. doi:https://doi.org/10.1016/B978-0-323-24272-1.00004-0.

Hyperion-Robotics (2021). *Post-tensioned 3d printed beam.*

J. Shah, T. C. S. K. M. L., B. Snider, & Hosseini, A. (2019). *Large-scale 3d printers for additive manufacturing: design considerations and challenges. The International Journal of Advanced Manufacturing Technology, 104*, 3679–3693. URL: https://link.springer.com/article/10.1007/s00170-019-04074-6#citeas. doi:https://doi.org/10.1007/s00170-019-04074-6.

John Corven, P.E. and Alan Moreton, P.E (2013). *Post-Tensioning Tendon Installation and Grouting Manual.* U.S. Department of Transportation, Federal Highway Administration.

Matmatch (2020). *Petg vs pla.* https://matmatch.com/learn/material/petg-vs-pla.

Mehdikhani, M., Gorbatikh, L., Verpoest, I., & Lomov, S. V. (2019). *Voids in fiber-reinforced polymer composites: A review on their formation, characteristics, and effects on mechanical performance. Journal of Composite Materials, 53*, 1579–1669. URL: https://doi.org/10.1177/0021998318772152. doi:10.1177/0021998318772152. arXiv:https://doi.org/10.1177/0021998318772152.

Post, B., Chesser, P., Lind, R., Roschli, A., Love, L., Gaul, K., Sallas, M., Blue, F., & Wu, S. (2018). *Using big area additive manufacturing to directly manufacture a boat hull mould. Virtual and Physical Prototyping, 14*, 1–7. doi:10.1080/17452759.2018.1532798.

Prusa Polymers (). *TECHNICAL DATA SHEET, Prusament PETG.* Prusa Research Prague, Czech Republic.

Prusa Research (2021). *Material guide, petg*. https://help.prusa3d.com/article/petg_2059.

Vantyghem, G., De Corte, W., Shakour, E., & Amir, O. (2020). *3d printing of a post-tensioned concrete girder designed by topology optimization. Automation in Con-*

struction, *112*, 103084. URL: https://www.sciencedirect.com/science/article/pii/S0926580519305096. doi:https://doi.org/10.1016/j.autcon.2020.103084.

Vladimir E. Kuznetsov, A. T. O. U. A. V., Alexey N. Solonin (2019). *Increasing strength of fff three-dimensional printed parts by influencing on temperaturerelated parameters of the process. Rapid Prototyping Journal*, *26*, 107–121.

Xunfei Zhou, Y. S., Sheng-Jen Hsieh (2017). *Experimental and numerical investigation of the thermal behaviour of polylactic acid during the fused deposition process. Virtual and Physical Prototyping*, *12*, 221–233. URL: https://doi.org/10.1080/17452759.2017.1317214. doi:10.1080/17452759.2017.1317214. arXiv:https://doi.org/10.1080/17452759.2017.1317214.

Yin, J., Lu, C., Fu, J., Huang, Y., & Zheng, Y. (2018). *Interfacial bonding during multi-material fused deposition modeling (fdm) process due to inter-molecular diffusion. Materials Design*, *150*, 104–112. URL: https://www.sciencedirect.com/science/article/pii/S0264127518302995. doi:https://doi.org/10.1016/j.matdes.2018.04.029.

Zhao, Y., Chen, Y., & Zhou, Y. (2019). *Novel mechanical models of tensile strength and elastic property of fdm am pla materials: Experimental and theoretical analyses. Materials Design*, *181*, 108089. URL: https://www.sciencedirect.com/science/article/pii/S0264127519305271. doi:https://doi.org/10.1016/j.matdes.2019.108089.

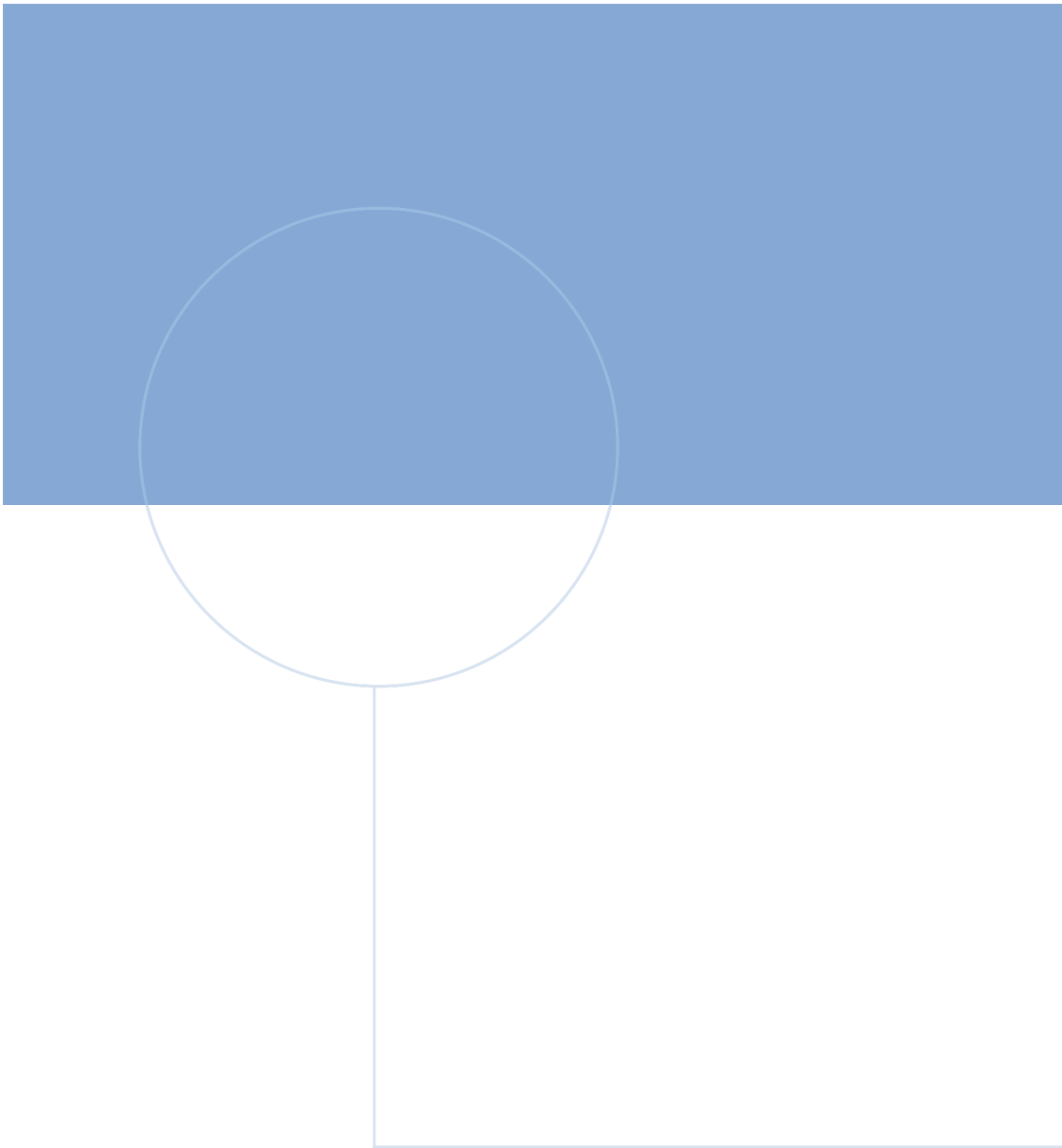

NTNU

Norwegian University of
Science and Technology